Global Observations of Deep Ocean Kinetic Energy Transfers

F. SÉVELLEC,[a,b] A. COLIN DE VERDIÈRE,[a] AND N. KOLODZIEJCZYK[a]

[a] *Laboratoire d'Océanographie Physique et Spatiale, Univ. Brest CNRS IRD Ifremer, Brest, France*
[b] *ODYSSEY Project-Team, INRIA CNRS, Brest, France*

(Manuscript received 31 July 2023, in final form 25 March 2024, accepted 5 April 2024)

ABSTRACT: Observations of deep Argo displacements (located between 950 and 1150 dbar) and their associated integrated Lagrangian velocities allow for the first time to compute worldwide deep horizontal transfers of kinetic energy (KE) between the $3^\circ \times 3^\circ$ mean and eddy reservoirs [mean kinetic energy (MKE) and eddy kinetic energy (EKE), respectively]. This diagnostic reveals that the transfers are mainly localized along western boundaries and in the Southern Ocean. Overall, the MKE-to-EKE transfers appear dominant globally and in all specifically tested regions (i.e., Gulf Stream, Kuroshio, Agulhas Current, and Antarctic Circumpolar Current). However, an important exception is the Zapiola Gyre where EKE-to-MKE transfers dominate. Beyond that, we find that horizontal KE transfers are better described by the horizontal properties of the mean flow deformation (divergence and strain) than by the horizontal properties of the turbulent velocities. Our theoretical analysis also demonstrates that the mean flow vorticity does not contribute to KE transfers. We show the existence of two consistent transfer modes: one from MKE to EKE and one from EKE to MKE, which are based on the eigendirections of the mean flow deformation tensor. The alignment of the turbulence along these directions selects the transfer modes, and it is the competition between these two transfer modes that leads to the actual transfers. We compute these transfer modes globally, regionally, and locally. We explain the distinctive situation of the Zapiola Gyre by the favored alignment of the turbulence with the EKE-to-MKE transfer mode. Overall, the dominance of the large-scale flow properties on the structure of the MKE-to-EKE transfers suggests the potential for large-scale parameterization.

KEYWORDS: Ocean circulation; Kinetic energy; Mesoscale processes; Nonlinear dynamics; Trajectories

1. Introduction

Ocean circulation acts on a wide range of time scales (Dijkstra 2000) from gravity waves to inertial motions (van Aken et al. 2007), to meso- and submesoscale turbulence (Chelton et al. 2007; McCoy et al. 2020), to Rossby waves (Tulloch et al. 2009), to long, climatically relevant basin-scale variability (Kushnir 1994). In particular, in energetic regions, such as the Gulf Stream, Kuroshio, Agulhas Current, Zapiola Gyre, and Antarctic Circumpolar Current, active mesoscale turbulence coexists with intense mean currents (e.g., van Sebille et al. 2011). Mean flow and eddy turbulence can feedback on each other because of nonlinear processes (Harrison and Robinson 1978). Hence, the interaction between the mean circulation and the eddy turbulence is a current topic of ocean research.

The subject of eddy-driven mean flows originated in the atmosphere when the midlatitude westerlies were shown through observations by Starr and collaborators (see Starr 1968) to be forced by the convergence of zonal momentum by the eddies. This has been confirmed by laboratory β-plane experiments showing the dynamical links between mean flow generation, Rossby wave radiation, and potential vorticity mixing (Whitehead 1975; Colin de Verdière 1979). Examples of such behaviors also exist in the ocean. For example, in the Gulf Stream, the transport estimated by the Sverdrup balance only accounts for a third of the actual transport. This remained a puzzle until quasigeostrophic models and theory showed the existence of inertial recirculation gyres forced by eddies produced by baroclinic instability (Holland 1978; Rhines and Holland 1979). Another example is the Zapiola Gyre in the Argentine Basin, whose circulation was first observed by Saunders and King (1995) during the WOCE experiment and has a barotropic transport around 120 Sv ($1\ \text{Sv} \equiv 10^6\ \text{m}^3\ \text{s}^{-1}$), as found from Argo float data by Colin de Verdière and Ollitrault (2016). The eddy-driven character of the circulation is discussed with both theory and numerical simulations by Dewar (1998) and de Miranda et al. (1999).

In this context, one of the current overarching questions of ocean dynamics is how the energy received by the ocean (Munk and Wunsch 1998) subsequently finds its way to dissipation through a wide range of scale interactions. Hence, the study of energy transfers has been a long, active field of ocean research using both local observations (e.g., Hall 1986; Rossby 1987, focusing on the Gulf Stream) and numerical models (e.g., Kang and Curchitser 2015). In an eddy-resolving high-resolution (1/10°) ocean model, von Storch et al. (2012) analyzed the energy budget following the Lorenz energy cycle (Lorenz 1955) in the absence of tidal forcing. They showed that most (~68%) of the kinetic energy (KE) dissipation was achieved through eddy kinetic energy (EKE) dissipation. Hence, the kinetic energy of the ocean [see Ferrari and Wunsch (2009) for a thorough review on kinetic energy in the ocean] and the distinction between mean kinetic energy (MKE) and EKE appear crucial. Arbic et al. (2014) further suggest the key role of eddy dynamics, which, through the inverse cascade of kinetic energy, generates long time-scale and large spatial-scale variability.

Observations of eddy–mean flow interactions have shown the existence of KE transfers between reservoirs (i.e., MKE reservoir and EKE reservoir). This has been computed in the Agulhas region by Zhu et al. (2018), for example. They show

Corresponding author: F. Sévellec, florian.sevellec@univ-brest.fr

DOI: 10.1175/JPO-D-23-0150.1

that the barotropic eddy energy conversion rate (i.e., transfers from MKE to EKE) is the main source of changes in the region, over the baroclinic eddy energy conversion rate (i.e., transfers from mean to eddy potential energy). In a more global and exhaustive framework, Chen et al. (2014a) derived a full energy transfer framework and showed the existence of local and nonlocal eddy–mean interactions (showing that the former dominates in the subtropics, whereas the latter dominates in intense current regions). This work has been extended by Chen et al. (2016) for time-dependent reservoirs. This leads to the identification of an additional KE reservoir [KE perturbation residual reservoir—residual kinetic energy (RKE) for residual KE], which acts as a buffer between MKE and EKE transfers. This rationalizes the effect of local and nonlocal eddy–mean interactions as transfers between MKE and EKE reservoirs and between MKE and RKE reservoirs, respectively. Beyond KE transfers, eddy–mean flow interactions have also been shown to impact tracer evolution (Marshall and Radko 2003), with consequences for long-term variability (Sévellec et al. 2021) and the interpretation of eddy-less ocean models (McDougall and McIntosh 2001).

Here, for the first time, we estimate from global deep observations the horizontal mean–eddy interactions and characterize the horizontal transfer of kinetic energy between the MKE and EKE reservoirs. For this purpose, we use velocities estimated from the Argo float deep displacement ANDRO database (Ollitrault et al. 2022). We show that the KE transfers at 1000-m depth are intensified along energetic western boundary currents and within the Antarctic Circumpolar Current. The transfers have a spatial scale significantly smaller than the mean flow. Decomposing the transfer based on the properties of the turbulent flow (isotropic, anisotropic, and covariance components) does not exhibit a dominant term. Also, the inherent coordinate dependence of this decomposition motivates the need for a coordinate-invariant decomposition. Hence, we suggest an alternative decomposition based on the mean flow properties (divergence and strain). It shows that the transfer is the small residual of two opposing and intense transfers: one from MKE to EKE and one from EKE to MKE acting along the horizontal strain directions. These transfers can be physically interpreted within the classical framework of eddy growth/decay. We find that the MKE-to-EKE transfer dominates globally, and in many regions, the Zapiola Gyre is an exception where the eddies drive the mean flow. If the eddy-driven character of the Zapiola Gyre has already been predicted from theory and numerical models (Dewar 1998; de Miranda et al. 1999), it is the first time that it is found in observations.

The article is organized as follows. The observational data and the method to infer mean and turbulent velocities are described in section 2. Section 3 presents the theoretical framework used to characterize KE transfers between the mean and eddy reservoirs. Results from the application of the framework to the observations are included in section 4. Conclusions are in section 5.

2. Data and methods

a. The ANDRO dataset

The ANDRO dataset provides horizontal velocities derived from Argo float deep displacements (Ollitrault et al. 2022). Details on the ANDRO dataset are provided in Ollitrault and Rannou (2013) and Ollitrault and Colin de Verdière (2014). We used the 2022 release corresponding to ANDRO_91950. Within this dataset, we have access to 1 347 392 velocity values since 2000. These velocities correspond to displacements of typically 10 days, which is set to represent the typical mesoscale turbulence decorrelation time (Freeland et al. 1975; Rossby et al. 1983; Owens 1991; Ollitrault and Colin de Verdière 2002).

From the full dataset, we first select velocities located at ~1000 dbar (within the range between 950 and 1150 dbar). This leads to a total of 1 000 981 displacements (Fig. 1). A full discussion of the sources of error is provided in Sévellec et al. (2017, 2022). Here, we will fully acknowledge these observational errors (also provided by the ANDRO dataset) by performing 10 successive, independent computations of the full analysis, following a Monte Carlo method (see the detailed description at the end of section 2b).

Before describing the methodology, it is important to acknowledge the horizontal inhomogeneity of the density of the Argo float displacements provided by the ANDRO dataset (Fig. 1). Velocities are recorded almost everywhere in the ocean, but the coverage shows lower density in the Southern Ocean and northern North Pacific and a relatively higher density in the South Pacific, North Atlantic, and central Indian Oceans. We computed the density of the selected Argo float displacements at each 1° × 1° location using a 3° × 3° size cell. The average density is 240 displacements per 3° × 3° with a standard deviation of 55 displacements per 3° × 3°, but it can locally go up to 1252 displacements per 3° × 3°.

In this framework, deviations from the mean flow within a 3° × 3° grid cell could be due to (permanent) spatial differences in the flow within the cell, time variations of the flow, or both. However, they are all used together to provide local velocity statistics. Hence, in the rest of the study, the mean will be defined as permanent features larger than 3° × 3°, whereas turbulence will be defined as spatiotemporally variable features smaller than 3° × 3° but longer than 10 days. This spatiotemporal average denotes the more classical spatial or temporal average often used to separate the mean and turbulent flows in the literature. This choice of a single spatiotemporal average is dictated by the observational dataset, but leads to a nontrivial interpretation of the mean and turbulent flows, as well as their interactions, that should be done carefully.

b. Methods

From these deep velocity observations, the mean velocity is computed for each 1° × 1° cell using a running average of all velocities over a 3° × 3° grid as

$$\overline{u}(x_0, y_0) = \frac{1}{n}\sum_{j=1}^{n} u_j(x,y)\Big|_{\mathcal{O}(x_0,y_0)}, \tag{1a}$$

$$\overline{v}(x_0, y_0) = \frac{1}{n}\sum_{j=1}^{n} v_j(x,y)\Big|_{\mathcal{O}(x_0,y_0)}, \tag{1b}$$

where x and y are the zonal and meridional coordinates, respectively; $\overline{u}$ and $\overline{v}$ are the mean zonal and meridional

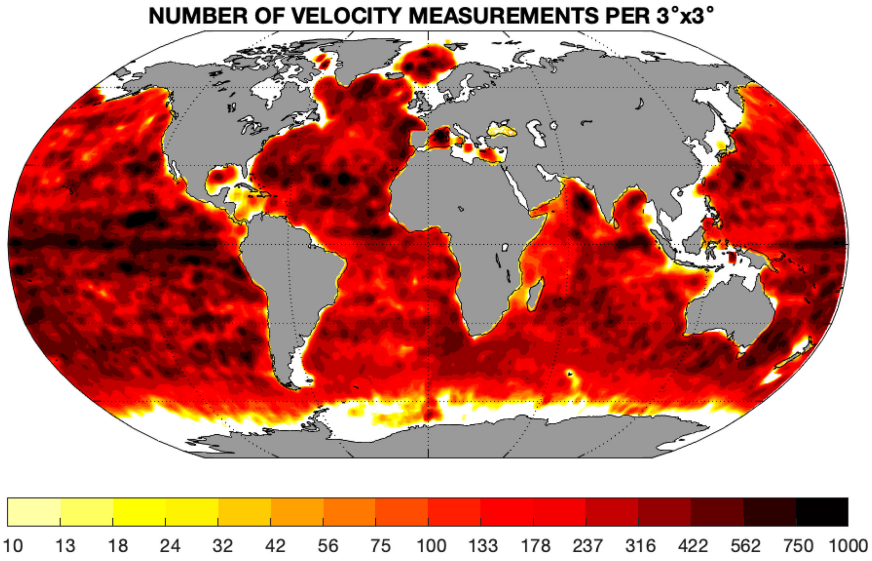

FIG. 1. Argo float deep displacement density. Number of velocity measurements from the ANDRO dataset per 3° × 3° cell along a 1° × 1° grid for the selected 1 000 981 velocities (i.e., between 950 and 1150 dbar). The color bar follows a log scale. The white colored regions correspond to regions with less than 10 measurements or no available data.

velocities, respectively; u_j and v_j are the zonal and meridional velocities from the ANDRO dataset, respectively; $\mathcal{O}(x_0, y_0)$ defines a cell centered at longitude x_0 and latitude y_0 such that $x \in [x_0 - (1/2)\Delta x, x_0 + (1/2)\Delta x]$ and $y \in [y_0 - (1/2)\Delta y, y_0 + (1/2)\Delta y]$ with x_0 and y_0 being evenly spaced every 1° and Δx and Δy being the zonal and meridional extents of the spatial mean corresponding to the 3° × 3° cell, respectively; n is the number of zonal and meridional velocity samples available in this $\mathcal{O}$ cell; and j is the index of these individual velocities.

The difference between the Eulerian mean and the Lagrangian mean is an old subject reviewed by Davis (1991). Regarding the specific issue of inferring velocities using Argo float trajectories, Wang et al. (2020) show that errors can reach up to 10% in numerical model estimates, differences which will not be further examined in the rest of the study. Beyond this, the locality of the velocity can also be questioned in fast current regions. Indeed, some Lagrangian particles can travel beyond a single grid cell over their 10-day displacement. In Sévellec et al. (2017), this was estimated to occur for 10% of the particles for a 4° × 4° grid. Hence, together with our reference 3° × 3° grid, we have tested the computation of KE transfers with three wider grids: 4° × 4°, 5° × 5°, and 6° × 6°. The grid size sets a scale selection differentiating the MKE and EKE reservoirs. We found that our results are robust to the grid size, beyond the typical smoothing expected with the use of wider grid (we refer the reader to section 5 and Fig. 14 for further discussion on this point).

The mean velocities show the general circulation at this depth (Figs. 2a,b). The circulation is dominated by an eastward flow in the Southern Ocean, characteristic of the Antarctic Circumpolar Current. The flow also shows signatures of intense circulation features such as the Gulf Stream, Kuroshio, Agulhas Current, and Zapiola Gyre, for instance.

From these mean velocities, we can compute the horizontal deformations caused by the mean flow. Following Okubo (1970) and Weiss (1991), we define four properties of the mean horizontal flow (Fig. 3):

$$\Delta = \partial_x \overline{u} + \partial_y \overline{v}, \tag{2a}$$

$$\zeta = \partial_x \overline{v} - \partial_y \overline{u}, \tag{2b}$$

$$\sigma_n = \partial_x \overline{u} - \partial_y \overline{v}, \tag{2c}$$

$$\sigma_s = \partial_x \overline{v} + \partial_y \overline{u}, \tag{2d}$$

where Δ is the divergence, ζ is the vorticity, σ_n is the stretching (or normal strain), and σ_s is the shearing (or shear strain). These diagnostics show that the divergence of the mean flow is small compared to the vorticity or strain, a result consistent with the expected underlying geostrophic dynamics. Note that the relatively large values of the divergence south of 56°S are occurring in regions where the sampling is the weakest and so should be taken with caution. Being spatial derivatives of the mean flow, large values of vorticity and strain are mainly located along intense western boundary currents and along the Antarctic Circumpolar Current. These diagnostics exhibit smaller spatial scales than the mean flow. The divergence and stretching show smaller-scale structures than the more coherent picture offered by the vorticity and shearing.

The turbulent velocities and velocity covariance (i.e., the horizontal Reynolds stresses) can also be estimated at each 1° × 1° cell as the standard deviation of all the velocities recorded in the ANDRO dataset within a 3° × 3° grid. This reads as follows:

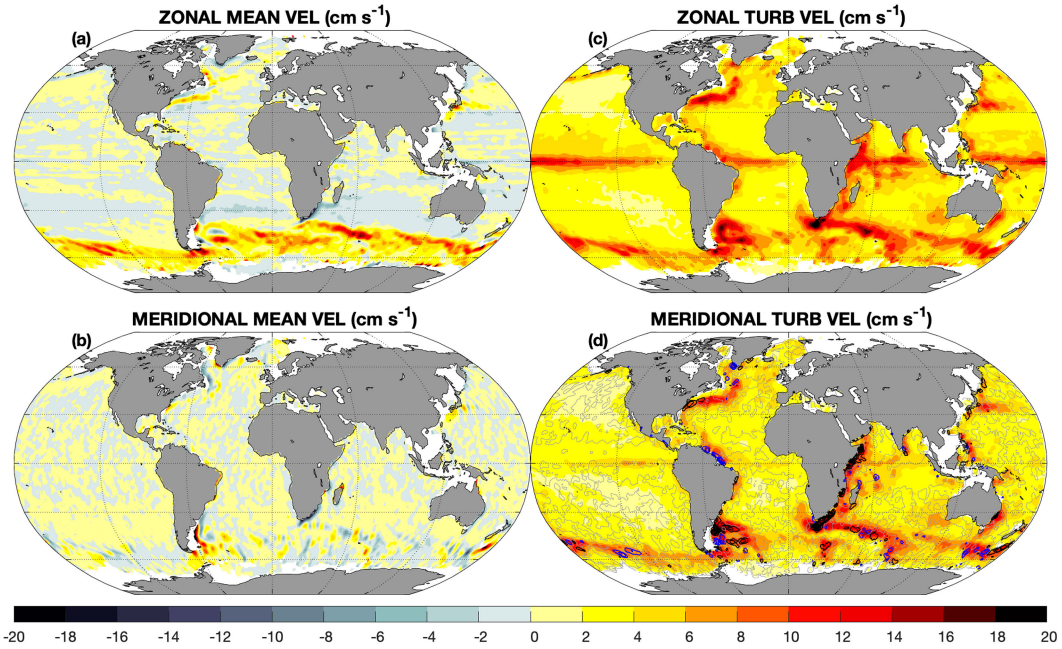

FIG. 2. Mean and turbulent zonal and meridional velocities. Colors show (a),(b) zonal and meridional mean and (c),(d) standard deviation of velocities (cm s^{-1}), following (1) and (3), respectively. The latter are a proxy for turbulent velocities. (d) Contours show covariance of zonal and meridional velocities, following (3). Velocities are computed as the velocity mean, standard deviation, and covariance within 3° × 3° cell on a 1° × 1° grid. Black, gray, and blue contours correspond to positive, zero, and negative values, with a contour interval of 20 cm^2 s^{-2}.

$$\tilde{u}(x_0, y_0) = \sqrt{\overline{u'^2}} = \sqrt{\frac{1}{n-1}\sum_{j=1}^{n}[u_j(x, y)|_{\mathcal{O}(x_0,y_0)} - \overline{u}]^2}, \quad (3a)$$

$$\tilde{v}(x_0, y_0) = \sqrt{\overline{v'^2}} = \sqrt{\frac{1}{n-1}\sum_{j=1}^{n}[v_j(x, y)|_{\mathcal{O}(x_0,y_0)} - \overline{v}]^2}, \quad (3b)$$

$$\tilde{c}(x_0, y_0) = \overline{u'v'} = \frac{1}{n-1}\sum_{j=1}^{n}[u_j(x, y)|_{\mathcal{O}(x_0,y_0)} - \overline{u}][v_j(x, y)|_{\mathcal{O}(x_0,y_0)} - \overline{v}], \quad (3c)$$

where $\overline{u'^2}$ and $\overline{v'^2}$ are the zonal and meridional velocity perturbation variances, respectively; $\tilde{u}$ and $\tilde{v}$ are the zonal and meridional standard deviations measuring the zonal and meridional turbulent velocities, respectively; and $\tilde{c}$ is the velocity covariance. From $\tilde{u}$ and $\tilde{v}$, we can define the eddy kinetic energy as $(\tilde{u}^2 + \tilde{v}^2)/2$. Given this definition, the turbulent velocities are not strictly restricted to mesoscale eddy turbulence and submesoscale processes, but include all variations found in the observations. Here, we should remind readers that we observe flows for frequencies lowest than Nyquist frequency ≃(0.05 cycles per day), with potential aliasing of higher-frequency processes.

Zonal and meridional turbulent velocities show intensification in western boundary currents and along the Antarctic Circumpolar Current (Figs. 2c,d), which are expected regions of intense turbulent mesoscale activity. The values in the Southern Ocean are consistent with the ones reported by Gille (2003; in the context of eddy momentum fluxes). The Zapiola Gyre and the Agulhas Current retroflection regions are also particularly energetic. The zonal turbulent velocities appear especially strong in the equatorial region (and are related to the meridional migration of mean currents and countercurrents, as well as equatorial wave dynamics; Brandt et al. 2011; Delpech et al. 2020). Hence, midlatitude turbulence is inhomogeneous, with strong values in western boundary currents and the Antarctic Circumpolar Current and weak values in the gyre interiors. There, it is mostly isotropic, while by contrast, the turbulence at the equator is strongly anisotropic with particular dominance of turbulent velocities over the mean velocities.

Consistent with the descriptions of Wunsch and Ferrari (2018), a Péclet number measured by the ratio of the mean to the standard deviation (i.e., reflecting the ratio of the mean advection to the turbulent advection) is smaller than 1 for our coarse 3° × 3° 1000-m depth flow (Figs. 2a,b vs Figs. 2c,d).

All the individual deep velocities (u_j and v_j) are associated with an observational error (u_j^* and v_j^*) provided by the ANDRO dataset (Ollitrault and Rannou 2013). These errors are used to estimate the robustness of our results through the Monte Carlo method. Hence, each individual Lagrangian velocity is treated as a random process with expectation value given by the observational data (u_j and v_j) and standard deviation given by the observational error (u_j^* and v_j^*). Ten realizations of random processes are carried out to create 10 independent datasets. The full analysis (binning on the regular 1° × 1° grid,

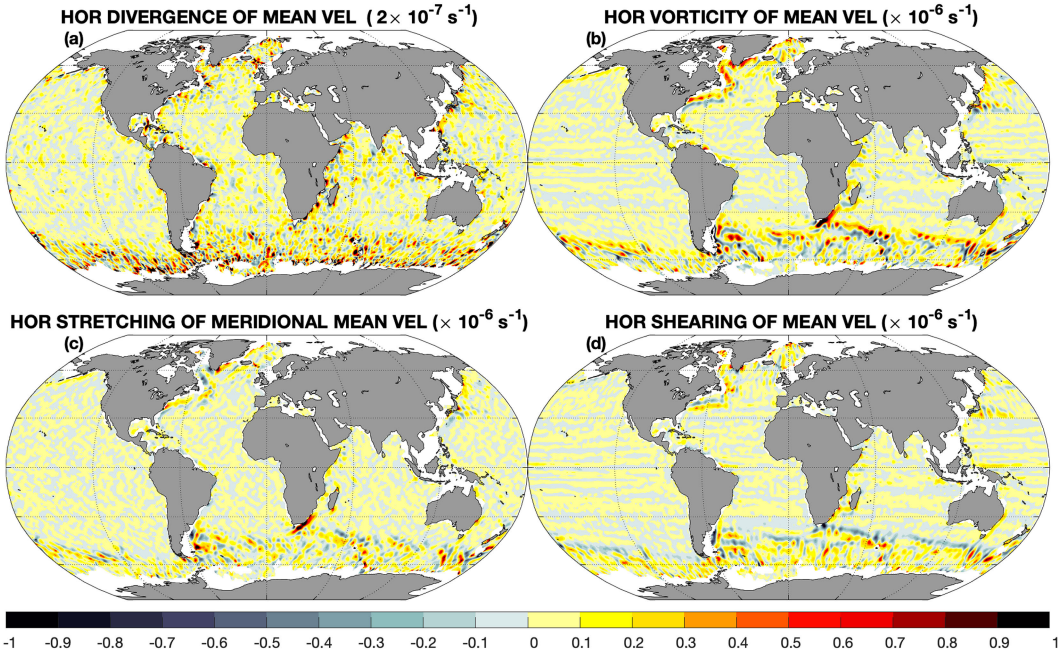

FIG. 3. Horizontal gradients of mean horizontal velocities. Colors show (a)–(d) horizontal divergence, vorticity, stretching (or normal strain), and shearing (or shear strain) of horizontal mean velocities.

computation of mean and turbulent velocity, and the computation of KE transfers described thereafter) is done for each realization. The mean and standard deviation of the results give the most likely result and its error, respectively. We stop after 10 realizations because the results and errors have converged. The convergence comes from the fact that KE transfers derive from the local velocity mean and standard deviation, which are well constrained despite the individual velocity errors, since we have an average of ~240 samples at each location (Fig. 1). The Monte Carlo realizations do not exhibit any visible changes in the patterns, so that the associated error is not shown in individual figures. It is only summarized in Table 1.

Despite not impacting the framework and derivations, since a mean and a standard deviation are defined without ambiguity regardless of the size of the dataset, the number of samples is another possible source of uncertainty. To test this source of truncation errors, we have reproduced the full analysis using two older releases of ANDRO: ANDRO_47029 and ANDRO_66657 from 2013 and 2019, respectively, which are still available online. By construction, they are such that

TABLE 1. Regional values of horizontal transfers of KE (10^{-11} m^2 s^{-3}). Values and uncertainties are averaged over the globe and five key regions: Gulf Stream, Kuroshio, Zapiola Gyre, Agulhas Current, and ACC. These regions have been chosen for their relatively intense KE transfers. The ACC region is defined as south of 35°S, whereas the others are shown in Fig. 4, for instance. The values and uncertainties are computed as the mean and the standard deviation of 10 Monte Carlo realizations. The relative values are the spatial integral of the region divided by the global area. Note that since negative values are possible, regional relative values can be high because of interregional compensations. The total horizontal transfers of KE are split into three terms based on turbulent flow properties: isotropic, anisotropic, and covariance. The total horizontal transfers are also split into properties of the mean flow: primary and secondary modes. Finally, the potential for MKE-to-EKE and EKE-to-MKE transfers ($\Phi_{MKE\to EKE}$ and $\Phi_{EKE\to MKE}$, respectively) and the efficiency of the MKE-to-EKE transfers ($\Gamma_{MKE\to EKE}$) are also indicated. Positive and negative values show MKE-to-EKE and EKE-to-MKE transfers, respectively. The dominant term for each of the categories/decompositions is shown in bold.

	Global	Gulf Stream	Kuroshio	Zapiola Gyre	Agulhas Current	ACC
Total (absolute)	**0.8** ± 0.0	**1.0** ± 0.1	**1.0** ± 0.2	**−1.4** ± 0.2	**11.5** ± 0.2	**2.9** ± 0.0
Total (relative)	100%	5%	7%	−7%	87%	97%
Isotropic	0.4 ± 0.0	**1.3** ± 0.1	0.2 ± 0.1	2.2 ± 0.1	5.8 ± 0.2	1.8 ± 0.1
Anisotropic	−0.3 ± 0.0	−1.2 ± 0.0	**0.7** ± 0.1	**−9.2** ± 0.2	−1.6 ± 0.2	−1.7 ± 0.1
Covariance	**0.7** ± 0.0	0.9 ± 0.0	0.1 ± 0.1	5.5 ± 0.1	**7.3** ± 0.1	**2.7** ± 0.1
Primary	**22.9** ± 0.2	**33.3** ± 0.1	**16.3** ± 0.3	97.7 ± 0.4	**88.2** ± 0.2	**57.2** ± 0.4
Secondary	−22.1 ± 0.2	−32.3 ± 0.2	−15.3 ± 0.2	**−99.2** ± 0.7	−76.7 ± 0.3	−54.3 ± 0.5
$\Phi_{MKE\to EKE}$	**44.0** ± 0.3	**66.0** ± 0.2	**30.9** ± 0.6	**193.6** ± 0.8	**167.3** ± 0.5	**110.8** ± 0.8
$\Phi_{EKE\to MKE}$	−43.2 ± 0.3	−63.4 ± 0.4	−30.5 ± 0.4	−189.2 ± 0.8	−155.7 ± 0.3	−107.1 ± 0.9
$\Gamma_{MKE\to EKE}$	0.50 ± 0.00	0.50 ± 0.00	0.50 ± 0.00	**0.49** ± 0.00	0.50 ± 0.00	0.50 ± 0.00

ANDRO_66657 (corresponding to a mean sample of ~180 per 3° × 3°) is a subsample of ANDRO_91950 and ANDRO_47029 (corresponding to a mean sample of ~100 per 3° × 3°) is a subsample of ANDRO_66657. This analysis confirms the robustness of our results and does not show a significant impact of the number of samples (not shown).

3. Analysis

a. Set of equations

To derive the horizontal kinetic energy transfers between the mean flow and its perturbation, we start from the Boussinesq, incompressible, primitive equations appropriate for a high Reynolds number (viscous forces are negligible), together with hydrostatic equilibrium for vertical momentum and nondivergence:

$$D_t u - fv = -\frac{1}{\rho_0}\partial_x p, \tag{4a}$$

$$D_t v + fu = -\frac{1}{\rho_0}\partial_y p, \tag{4b}$$

$$0 = -\frac{1}{\rho_0}\partial_z p - \frac{g}{\rho_0}\rho, \tag{4c}$$

$$\partial_x u + \partial_y v + \partial_z w = 0, \tag{4d}$$

where t, x, y, and z are the time, longitude, latitude, and depth, respectively; u, v, and w are the zonal, meridional, and vertical velocities, respectively; $\rho_{(0)}$ is the (reference) density for seawater; p is the pressure; f is the Coriolis parameter; g is the acceleration due to gravity; and $(D_t = \partial_t + u\partial_x + v\partial_y + w\partial_z)$ is the material derivative.

b. Mean and eddy kinetic energy evolution

From this set of equations, we can derive the evolution of mean and eddy kinetic energy. This derivation can be found in some forms in numerous previous studies or textbooks (e.g., Rossby 1987; Davidson 2004). It is summarized here for consistency and to provide the readers with the exact framework.

Splitting the velocities, density, and pressure between a (spatiotemporal) mean ($\overline{\cdot}$) and a perturbation ($'$) from this mean such that $u = \overline{u} + u'$, $v = \overline{v} + v'$, $w = \overline{w} + w'$, $\rho = \overline{\rho} + \rho'$, and $p = \overline{p} + p'$ (with $\overline{u'} = \overline{v'} = \overline{w'} = 0$, $\overline{\rho'} = 0$, and $\overline{p'} = 0$), we obtain a set of equations for the mean and a set of equations for the perturbation. Then, we can write the mean evolution of MKE [defined as $(\overline{u}^2 + \overline{v}^2)/2$] as

$$\begin{aligned}\overline{D}_t\mathrm{MKE} = &-\overline{u}(\partial_x\overline{u'^2} + \partial_y\overline{u'v'} + \partial_z\overline{u'w'})\\ &-\overline{v}(\partial_x\overline{u'v'} + \partial_y\overline{v'^2} + \partial_z\overline{v'w'})\\ &-\frac{g}{\rho_0}\overline{w}\overline{\rho} - \frac{1}{\rho_0}(\overline{u}\partial_x\overline{p} + \overline{v}\partial_y\overline{p} + \overline{w}\partial_z\overline{p}),\end{aligned} \tag{5}$$

where $\overline{D}_t$ is the mean material derivative $(= \partial_t + \overline{u}\partial_x + \overline{v}\partial_y + \overline{w}\partial_z)$. The first two lines correspond to the eddy–mean flow interactions, whereas the third line corresponds to the mean baroclinic transfer with potential energy and the mean pressure work.

We define the eddy–mean interactions acting on MKE as

$$\begin{aligned}\mathcal{C} = &-\overline{u}(\partial_x\overline{u'^2} + \partial_y\overline{u'v'} + \partial_z\overline{u'w'})\\ &-\overline{v}(\partial_x\overline{u'v'} + \partial_y\overline{v'^2} + \partial_z\overline{v'w'}).\end{aligned} \tag{6}$$

The two terms within the parentheses are the divergence of the Reynolds stresses, the turbulent forces acting on the mean circulation. Hence, $\mathcal{C}$ is the work of these forces, corresponding to the action of the turbulence on the mean flow.

Following the same steps as for the MKE but starting from the set of equations for the perturbation, the EKE [defined as $(\overline{u'^2} + \overline{v'^2})/2$] changes read

$$\begin{aligned}\overline{D_t\mathrm{EKE}} = &-(\overline{u'^2}\partial_x\overline{u} + \overline{v'^2}\partial_y\overline{v})\\ &-\overline{u'v'}(\partial_x\overline{v} + \partial_y\overline{u}) - \overline{u'w'}\partial_z\overline{u} - \overline{v'w'}\partial_z\overline{v}\\ &-\frac{g}{\rho_0}\overline{w'\rho'} - \frac{1}{\rho_0}(\overline{u'\partial_x p'} + \overline{v'\partial_y p'} + \overline{w'\partial_z p'}).\end{aligned} \tag{7}$$

On the left-hand side of this equation is the mean of the time evolution together with the advection by the mean velocity and by the velocity perturbation of EKE. These advective terms, which include eddy–mean interactions, are divergence terms that vanish by integration over the domain. Hence, they redistribute EKE, but are not a net source or sink of EKE, per se. On the right-hand side of this expression, we have sources and sinks of EKE. The first two lines correspond to eddy–mean flow interactions, where the two first terms are horizontal transfers from the mean kinetic energy (as demonstrated later) and the two following ones are vertical transfers from the mean kinetic energy. The third line corresponds to baroclinic transfer with potential energy and pressure gradient work.

Equivalently to the evolution of MKE, we define the eddy–mean interactions acting on EKE as

$$\begin{aligned}\mathcal{B} = &-(\overline{u'^2}\partial_x\overline{u} + \overline{v'^2}\partial_y\overline{v}) - \overline{u'v'}(\partial_x\overline{v} + \partial_y\overline{u})\\ &-\overline{u'w'}\partial_z\overline{u} - \overline{v'w'}\partial_z\overline{v}.\end{aligned} \tag{8}$$

c. Local versus nonlocal eddy–mean interactions

Using integration by parts, the eddy–mean interaction terms for MKE [(6)] can be rearranged to explicitly show the link between the evolution of EKE and MKE. We obtain

$$\begin{aligned}\mathcal{C} = &(\overline{u'^2}\partial_x\overline{u} + \overline{v'^2}\partial_y\overline{v}) + \overline{u'v'}(\partial_x\overline{v} + \partial_y\overline{u}) + \overline{u'w'}\partial_z\overline{u} + \overline{v'w'}\partial_z\overline{v}\\ &-[\overline{u'\partial_x(\overline{u}u')} + \overline{v'\partial_y(\overline{u}u')} + \overline{w'\partial_z(\overline{u}u')}]\\ &-[\overline{u'\partial_x(\overline{v}v')} + \overline{v'\partial_y(\overline{v}v')} + \overline{w'\partial_z(\overline{v}v)}].\end{aligned} \tag{9}$$

We find $\mathcal{C} = -\mathcal{B} + \mathcal{D}$, where $\mathcal{D}$ can be rewritten as a divergence term using (4d), the second and third line in (9). Here,

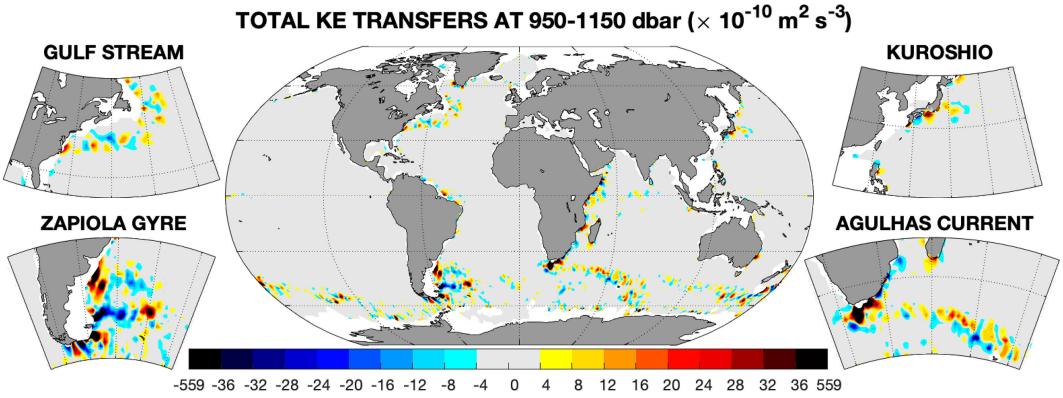

FIG. 4. Total horizontal transfers of KE. The total horizontal transfers of KE ($\{\text{MKE} \leftrightarrow \text{EKE}\}_{\text{hor}}$) is computed following (10). Positive and negative values show MKE-to-EKE and EKE-to-MKE transfers, respectively. Insets (clockwise from top left) show magnification for the Gulf Stream, Kuroshio, Agulhas Current, and Zapiola Gyre regions.

$-\mathcal{B}$ represents the horizontal and vertical sources and sinks of MKE, which also appear in the EKE evolution [(8)], with the opposite sign (consistent with the description of Tennekes and Lumley 1972, for instance). Hence, it corresponds to the kinetic energy transfer between MKE and EKE reservoirs. The second term $\mathcal{D}$ represents the perturbation advection of residual kinetic energy (defined as $\text{RKE} = \overline{u}u' + \overline{v}v'$). It is equivalent to an eddy-induced advection of first-order kinetic energy perturbation. This term has no net global impact since it is a divergence of a flux, which is zero at the boundaries (and after acknowledging the nondivergence of the eddy flow). This corresponds to a geographical redistribution of kinetic energy. Hence, the domain average of $\mathcal{C}$ and $-\mathcal{B}$ is equal and opposite. Following Chen et al. (2014a, 2016), the terms $-\mathcal{B}$ and $\mathcal{D}$ are called local and nonlocal mean–eddy interaction, respectively. Since the goal of the study is to assess kinetic energy transfers, we will focus exclusively on the local mean–eddy interactions $\mathcal{B}$.

4. Results

a. *Global observations of horizontal kinetic energy transfers*

In the context of velocity gathered by deep displacements of Argo floats from the ANDRO database, the whole expression of the evolution of mean and eddy kinetic energy cannot be fully assessed. Indeed, the Argo floats only give us access to the horizontal velocities. This means that the vertical transfers of kinetic energy and the baroclinic transfers with potential energy cannot be evaluated. Note that away from the equator, the vertical kinetic energy transfers are expected to be smaller than the horizontal ones given the small Rossby number of the large-scale circulation and mesoscale turbulence. The baroclinic transfers from available potential energy are obviously significant since the main source of turbulence at mesoscale is the conversion of mean potential energy by baroclinic instability. Other terms such as the pressure gradient term, the advection by the mean flow, and the advection by the turbulence vanish by integration over the domain. They transport MKE or EKE but have no net contribution.

Hence, we will focus in the rest of the study on the horizontal component of KE transfers, which, following (8), reads

$$\{\text{MKE} \leftrightarrow \text{EKE}\}_{\text{hor}} = \mathcal{B}|_{\text{hor}} = -(\overline{u'^2}\partial_x\overline{u} + \overline{v'^2}\partial_y\overline{v}) - \overline{u'v'}(\partial_x v + \partial_y\overline{u}). \quad (10)$$

This term will be referred to as KE transfers. Here, positive and negative values correspond to net transfers from MKE to EKE and from EKE to MKE.

Using this diagnostic, we find that the major transfers are located in western boundary regions, the equator, and the Southern Ocean (Fig. 4). Particularly, active regions are associated with intense current and eddy-active regions (Fig. 2 vs Fig. 4): the Gulf Stream, the Kuroshio, the Zapiola Gyre, the Agulhas Current, and the Antarctic Circumpolar Current. KE transfer values in these regions could go up to $\pm 560 \times 10^{-10}$ m^2 s^{-3} with important spatial and amplitude variations (Figs. 4 and 5a, respectively). Regional spatial mean values are residuals of large positive and negative values (Fig. 5a). The global mean transfer is positive with a value of $+0.8 \times 10^{-11}$ m^2 s^{-3}. All abovementioned regions have also a net positive MKE-to-EKE transfer value ($+1.0 \times 10^{-11}$, $+1.0 \times 10^{-11}$, $+11.5 \times 10^{-11}$, and $+2.9 \times 10^{-11}$ m^2 s^{-3} for the Gulf Stream, the Kuroshio, the Agulhas Current, and the Antarctic Circumpolar Current, respectively; Table 1), except the Zapiola Gyre, where the EKE-to-MKE transfers dominate (-1.4×10^{-11} m^2 s^{-3}, Table 1). Using 10 realizations following the Monte Carlo method, we have tested the robustness of these results, which exhibit excellent accuracy (Table 1).

For all tested regions, their relative contributions (far) exceed their relative area (Table 1). This suggests that they are key regions of KE transfers. In particular, at the studied depth, the Agulhas Current and the Antarctic Circumpolar Current (ACC) have relative contributions close to the total global KE transfers.

Deep observations of KE transfers are rare, so comparisons of our results with previously established data are limited. In

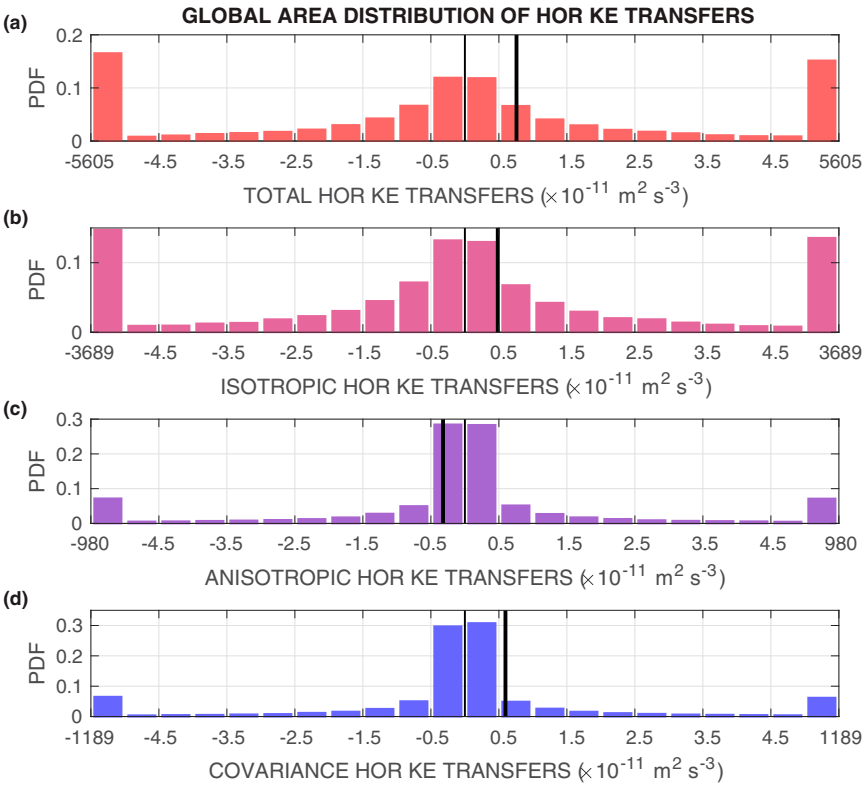

FIG. 5. Distribution of horizontal transfers of KE. Distribution of (a) total and (b) isotropic, (c) anisotropic, and (d) covariance horizontal transfer components of KE. The total horizontal transfer of KE ($\{\text{MKE} \leftrightarrow \text{EKE}\}_{\text{hor}}$) is computed following (10), and the components follow the decomposition of (11), based on the properties of the turbulent flow. Positive and negative values show MKE-to-EKE and EKE-to-MKE transfers, respectively. The vertical black lines correspond to the global mean for each component. Note that the large values of the extreme bins are because of the large range of the extreme bins, not because of frequent large outliers.

the Southern Ocean, south of Tasmania (50°S–143°E), Phillips and Rintoul (2000) reported a value of $(1.6 \pm 9.4) \times 10^{-9}\ \text{m}^2\ \text{s}^{-3}$ using 2-yr-long velocity measurements from moorings. We also find that this region exhibits particularly intense MKE-to-EKE transfers (Fig. 4). Beyond the large uncertainties described in Phillips and Rintoul (2000), we obtain values consistent with theirs (of the order of a few $10^{-9}\ \text{m}^2\ \text{s}^{-3}$).

b. *Physical turbulent components of kinetic energy transfers*

To better understand the physical constraints of the transfers, we first decomposed the following properties of horizontal turbulence:

$$\begin{aligned}\{\text{MKE} \leftrightarrow \text{EKE}\}_{\text{hor}} = &-\frac{1}{2}(\overline{u'^2} + \overline{v'^2})(\partial_x \overline{u} + \partial_y \overline{v})\\ &-\frac{1}{2}(\overline{u'^2} - \overline{v'^2})(\partial_x \overline{u} - \partial_y \overline{v})\\ &-\overline{u'v'}(\partial_x \overline{v} + \partial_y \overline{u})\cdot \end{aligned} \tag{11}$$

This decomposition follows the decomposition suggested by Hoskins et al. (1983) in the context of eddy momentum transfers. These three components are also associated with different properties of the mean flow.

1) The transfers by the isotropic component of the turbulence act through the horizontal divergence of the mean flow:

$$-\overline{\text{EKE}}\,\Delta. \tag{12a}$$

2) The transfers by the anisotropic component of the turbulence act through the horizontal stretching (or normal strain) of the mean flow:

$$-\frac{1}{2}(\overline{u'^2} - \overline{v'^2})\sigma_n. \tag{12b}$$

3) The transfers by the covariance component of the turbulence act through the horizontal shearing (or shear strain) of the mean flow:

$$-\overline{u'v'}\sigma_s. \tag{12c}$$

Note that there is no explicit contribution of the mean flow vorticity here (as will be explicitly demonstrated later), even though stability theorems involve the gradient of mean potential vorticity.

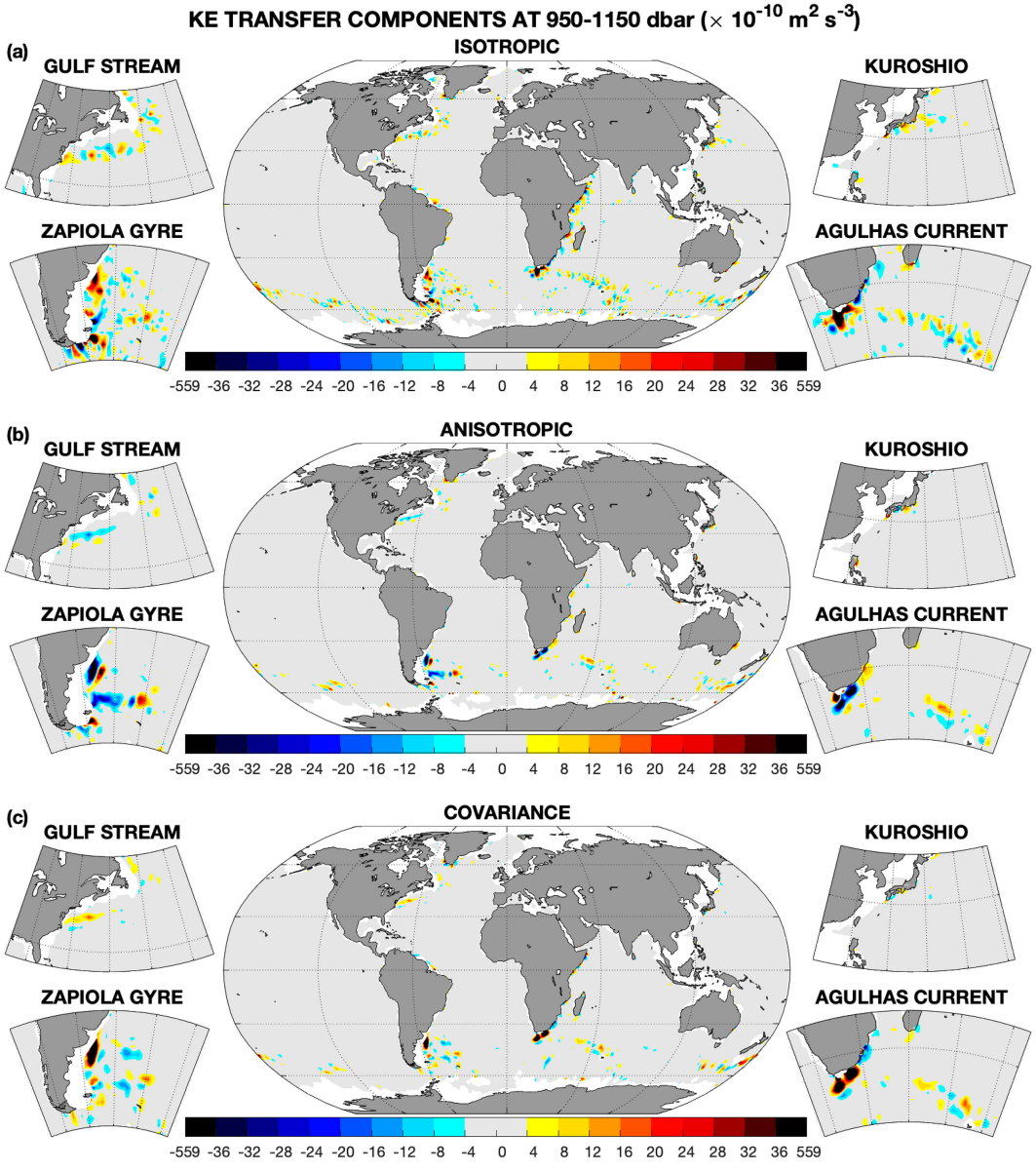

FIG. 6. Components of horizontal transfers of KE. As in Fig. 4, but for each of the KE transfer components of the decomposition (12), based on turbulent flow properties: (a) isotropic, (b) anisotropic, and (c) covariance components. Positive and negative values show MKE-to-EKE and EKE-to-MKE transfers, respectively. Insets (clockwise from top left) show magnification for the Gulf Stream, Kuroshio, Agulhas Current, and Zapiola Gyre regions.

Following (11), we compute the three components of the total horizontal transfers. This shows that the three components remain spatially variable (Fig. 6). The geographical maps do not show clear dominance of one component over the others, except maybe slightly larger values of the component related to the isotropic turbulence. The statistical distributions of these three components reveal that the isotropic component mainly controls the shape of the statistical distribution of the total transfer, whereas the anisotropic and covariance components exhibit lower values and tighter distributions (Fig. 5). These tighter distributions are consistent with the relatively good spatial consistency of the anisotropic and covariance components compared to the isotropic ones (e.g., Gulf Stream or Agulhas Current regions in Fig. 6). The global mean values correspond to an MKE-to-EKE transfer for the isotropic and covariance components, whereas it is an EKE-to-MKE transfer for the anisotropic component (Fig. 5 and Table 1). The global mean of total transfers is mainly controlled by its covariance component (Table 1).

For the four specifically studied regions, we find that the dominant term hugely varies from region to region (Table 1). As for the global mean, the anisotropic term appears to be

the only component able to drive an EKE-to-MKE transfer in regional averages. However, it drives MKE-to-EKE transfer in the Kuroshio region, where it is the dominating component. The dominant term is the isotropic, anisotropic, and covariance components in the Gulf Stream, Zapiola Gyre, and Agulhas Current regions, respectively. The covariance component also dominates in the Antarctic Circumpolar Current region. However, overall, the decomposition in properties of the turbulent flow does not help us disentangle a general role for each component. Following this conclusion, we suggest an alternative approach to decompose the horizontal transfers of kinetic energy.

c. *Natural mean components of kinetic energy transfers*

1) DECOMPOSITION

Using (12), we have computed the three horizontal KE transfer terms and have assessed their respective importance. Here, we will suggest a new decomposition based on the idea that the mean strain tensor is key for eddy–mean flow interactions (Tennekes and Lumley 1972) and that eddies grow and decay along strain directions (Kundu 1990). Hence, in this framework, it is interesting to note that the horizontal transfers can be rewritten in the form of a scalar product of velocity perturbations transformed by the mean velocity gradients. This reads

$$\begin{aligned}\{\mathrm{MKE}\leftrightarrow\mathrm{EKE}\}_{\mathrm{hor}} &= -(\overline{u'^2}\partial_x\overline{u} + \overline{v'^2}\partial_y\overline{v}) - \overline{u'v'}(\partial_x\overline{v} + \partial_y\overline{u}),\\ &= \overline{(u',\,v')\begin{pmatrix}-\partial_x\overline{u} & -\partial_x\overline{v}\\ -\partial_y\overline{u} & -\partial_y\overline{v}\end{pmatrix}\begin{pmatrix}u'\\ v'\end{pmatrix}},\\ &= \overline{(u',\,v')\begin{bmatrix}-\frac{1}{2}(\Delta+\sigma_n) & -\frac{1}{2}(\sigma_s+\zeta)\\ -\frac{1}{2}(\sigma_s-\zeta) & -\frac{1}{2}(\Delta-\sigma_n)\end{bmatrix}\begin{pmatrix}u'\\ v'\end{pmatrix}}.\end{aligned} \tag{13}$$

The mean velocity gradient tensor is the exact same operator as the Jacobian matrix for horizontal tracer gradients described by Okubo (1970) and Weiss (1991). We can split the tensor into symmetric and skew-symmetric parts. This is interesting since the former is related to deformation and the latter to rotation. This reads

$$-\frac{1}{2}\begin{pmatrix}\Delta+\sigma_n & \sigma_s+\zeta\\ \sigma_s-\zeta & \Delta-\sigma_n\end{pmatrix} = -\frac{1}{2}\begin{pmatrix}\Delta+\sigma_n & \sigma_s\\ \sigma_s & \Delta-\sigma_n\end{pmatrix} - \frac{1}{2}\begin{pmatrix}0 & \zeta\\ -\zeta & 0\end{pmatrix},$$

where the symmetric part is the mean flow deformation tensor (or mean strain tensor). It corresponds to the divergence, the shearing, and the stretching of the mean flow (Δ, σ_s, and σ_n, respectively), and the skew-symmetric part corresponds solely to the vorticity of the flow ζ. Applying them independently to the velocity perturbations reveals that only the symmetric part of the tensor has an action, since the skew-symmetric component leads to a vanishing transfer. This demonstrates that the vorticity of the mean flow does not transfer kinetic energy, but only transfers variance between zonal and meridional directions within a reservoir. It is also useful to discuss the symmetric part of the tensor under the geostrophic assumption. Since the geostrophic flow is nondivergent on an f plane, the transfer will only be controlled by the strain terms and the trace of the tensor would be zero. This means that with an isotropic turbulence ($\overline{u'^2} = \overline{v'^2}$), the transfers would only occur through the covariance of the turbulence. Hence, the existence of transfer is linked to either the ageostrophy of the mean flow, the horizontal anisotropy or covariance of the turbulence, the β effect, or a combination of the above.

This formulation of the transfer through the symmetric tensor is also interesting because it allows us a simpler decomposition. Indeed, symmetric tensors have eigenvectors that are orthogonal to each other, precluding us from the need to compute biorthogonal eigenvectors (e.g., Farrell and Ioannou 1996a,b). Hence, one can write, without loss of generality,

$$\{\mathrm{MKE}\leftrightarrow\mathrm{EKE}\}_{\mathrm{hor}} = \overline{(u',\,v')\begin{pmatrix}-\frac{1}{2}(\Delta+\sigma_n) & -\frac{1}{2}\sigma_s\\ -\frac{1}{2}\sigma_s & -\frac{1}{2}(\Delta-\sigma_n)\end{pmatrix}\begin{pmatrix}u'\\ v'\end{pmatrix}}, \tag{14}$$

$$= \overline{(u',\,v')\begin{pmatrix}\hat{p}_x & \hat{s}_x\\ \hat{p}_y & \hat{s}_y\end{pmatrix}\begin{pmatrix}\lambda_p & 0\\ 0 & \lambda_s\end{pmatrix}\begin{pmatrix}\hat{p}_x & \hat{p}_y\\ \hat{s}_x & \hat{s}_y\end{pmatrix}\begin{pmatrix}u'\\ v'\end{pmatrix}}, \tag{15}$$

where $(\hat{p}_x,\,\hat{p}_y)$ and $(\hat{s}_x,\,\hat{s}_y)$ are the eigenvectors associated with the eigenvalues λ_p and λ_s, respectively, of the mean flow deformation tensor, so that $\hat{p}_x\hat{p}_x + \hat{p}_y\hat{p}_y = \hat{s}_x\hat{s}_x + \hat{s}_y\hat{s}_y = 1$ and $\hat{p}_x\hat{s}_x + \hat{p}_y\hat{s}_y = 0$. This shows that the velocity perturbations are rotated within or projected onto the natural directions of the deformation of the mean flow [$(\hat{p}_x,\,\hat{p}_y)$ and $(\hat{s}_x,\,\hat{s}_y)$] where a deformation of amplitude λ_p or λ_s is applied.

The eigenvalues of the symmetric matrix [(14)] are

$$\lambda_{p/s} = -\frac{1}{2}\Delta \pm \frac{1}{2}\sigma, \tag{16}$$

where σ is the strain magnitude, such that $\sigma^2 = \sigma_s^2 + \sigma_n^2$. This expression is particularly useful since both the divergence and the strain magnitude are coordinate invariant (i.e., intrinsic kinematic quantities). Here, the primary and secondary eigenvalues differ by the constructive or opposing action of the strain magnitude on the horizontal divergence. Hence, in the absence of strain ($\sigma = 0$), the eigenvalues become half the divergence: $\lambda_p = \lambda_s = -\Delta/2$. In the absence of horizontal divergence ($\Delta = 0$), the eigenvalues act to both transfers from MKE to EKE and from EKE to MKE equivalently with $\lambda_{p/s} = \pm\sigma/2$ acting along their respective eigenvector direction. It is also worth noting that the sum of the two eigenvalues is the horizontal divergence (since the trace is conserved). The eigenvectors associated with the eigenvalue $\lambda_{p/s}$ are $(\sigma_n \mp \sigma,\,\sigma_s)/\sqrt{2\sigma^2 \mp 2\sigma\sigma_n}$, and this expression is slightly more complex and reincorporates σ_s and σ_n, which are not coordinate invariant, allowing the nontrivial definition of a direction. These orthogonal eigenvectors correspond to the two natural

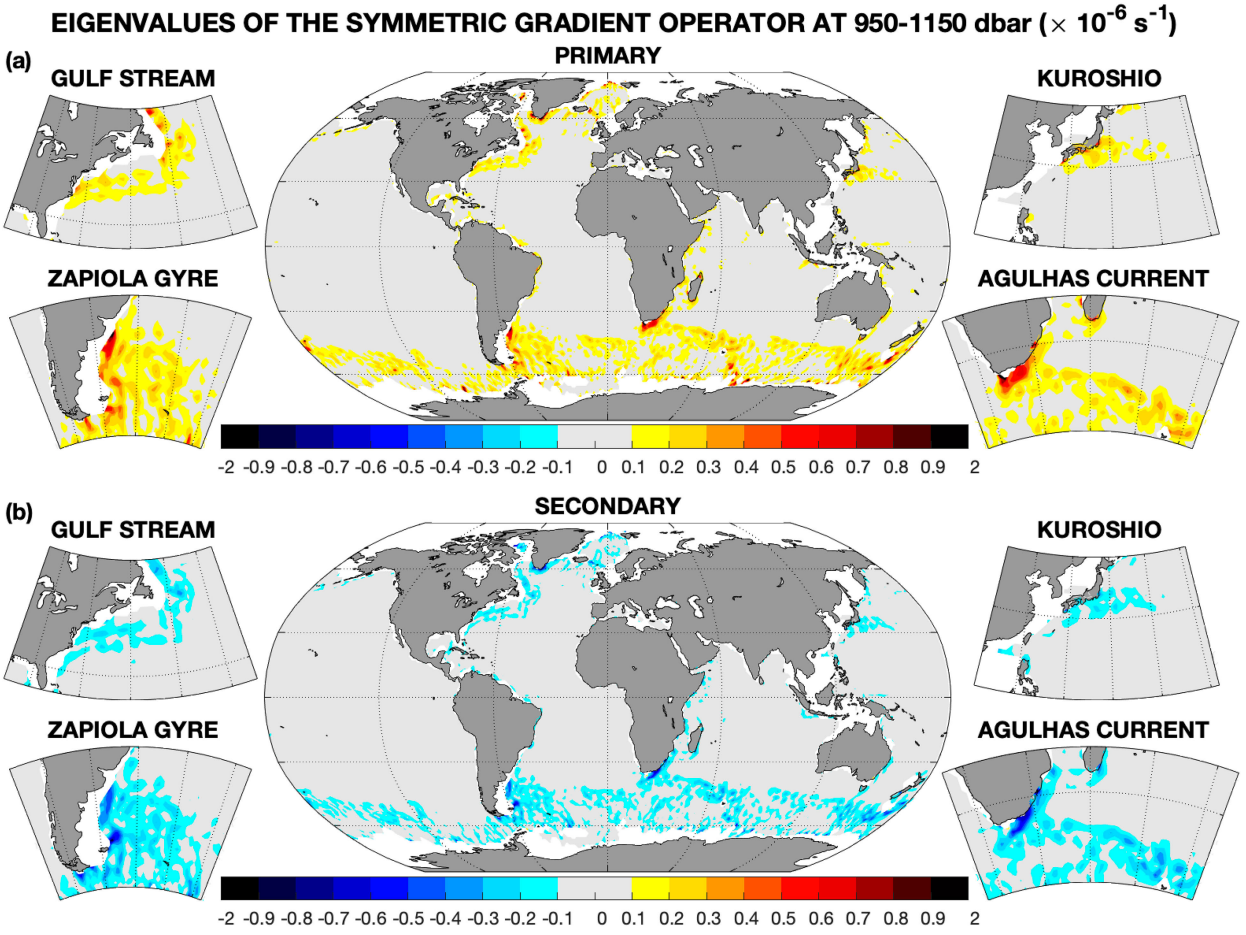

FIG. 7. Eigenvalues of the symmetric operator of the mean flow gradients. Eigenvalues for the (a) primary and (b) secondary modes, following the decomposition of (15) and expression of (16). Positive and negative values are associated with transfers from MKE to EKE and from EKE to MKE, respectively. The maximum (2×10^{-6} s^{-1}) and color increment (10^{-7} s^{-1}) correspond to time scales of 5.8 and 115.7 days, respectively. The sum of the eigenvectors corresponds to the horizontal divergence of the mean flow (Fig. 3a). Insets (clockwise from top left) show magnification for the Gulf Stream, Kuroshio, Agulhas Current, and Zapiola Gyre regions.

directions of deformation of the mean flow. For example, within a purely strain dynamics, they are the directions of convergence and divergence of the flow, corresponding to directions of concentration and of spreading of passively advected particles (e.g., Okubo 1970).

Applied to our dataset, the eigenvalues exhibit values in the range $\pm 2 \times 10^{-6}$ s^{-1}, which corresponds to times longer than 5.8 days (Fig. 7). The primary eigenvalues are almost exclusively positive values everywhere, leading to MKE-to-EKE transfers, whereas the secondary eigenvalues are almost exclusively negative values everywhere, leading to EKE-to-MKE transfers. These values are particularly strong in energetic regions, such as western boundaries, especially where intense, turbulent currents occur, and in the Southern Ocean. On the other hand, the ocean interior exhibits low eigenvalues. The values of each eigenvalue are quite high (of the order of 10^{-6} s^{-1}) compared to their sum (10^{-7} s^{-1}). This suggests, as expected for a weakly divergent horizontal flow, that the mean flow is mainly strain dominated ($\sigma > |\Delta|$) or even significantly strain dominated ($\sigma \gg |\Delta|$) in most regions (Fig. 8). This means that there is a significant compensation of the action of the two eigenvectors.

This eigenvector decomposition allows us to define a primary and secondary source of kinetic energy transfers linked to the primary and secondary directions of the deformation of the mean flow. Following (15), this reads

$$\{\mathrm{MKE} \leftrightarrow \mathrm{EKE}\}_{\mathrm{hor}} = \lambda_p \overline{(u'\hat{p}_x + v'\hat{p}_y)^2} + \lambda_s \overline{(u'\hat{s}_x + v'\hat{s}_y)^2}, \tag{17}$$

where the first and second terms of the right-hand side correspond to the primary and secondary directions, respectively. Since $\lambda_p > \lambda_s$ and the mean flow is mainly strain dominated ($\sigma > |\Delta|$), the primary and secondary directions mainly lead to MKE-to-EKE and EKE-to-MKE transfers, respectively. This split between EKE to MKE and MKE to EKE is unique, being set by the equations controlling the evolution of the momentum. Hence, here, we have a dynamical

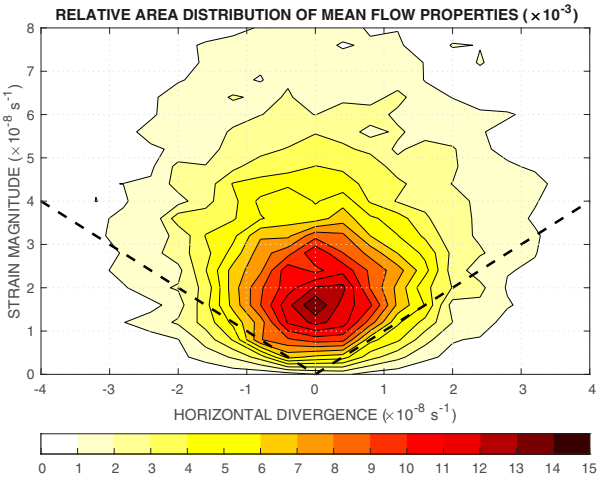

FIG. 8. Strain magnitude vs horizontal divergence. Relative distribution of the mean horizontal flow in terms of its strain magnitude and of its divergence. The dashed lines correspond to $\sigma = |\Delta|$, separating regions dominated by strain or divergence. This reveals the (strong) dominance in most regions of strain in setting the eigenvalues as two intense positive and negative values compared to their sum (the trace), which corresponds to the divergence. The spatial integral of the distribution is set to be one.

attribution of KE transfers. Note that the primary component could be weaker in absolute values than the secondary component.

This decomposition through the primary and secondary components allows us to separate MKE-to-EKE and EKE-to-MKE transfers from the total transfers (Fig. 9). This suggests the importance of this decomposition based on the natural properties of the mean flow (compared to the decomposition based on the physical properties of the turbulent flow). Hence, the primary and secondary transfers correspond to a spatially consistent pattern, where the transfers mainly occur along western boundaries, through intense boundary currents, and in the Southern Ocean. The global mean values of each of these transfers are one order of magnitude higher than their sum (Table 1). This suggests that the total transfers are small residuals of the primary and secondary components, or, in other words, the total transfers are small outcomes of the competition between large MKE-to-EKE and EKE-to-MKE transfers. Spatial averages show that the primary component (associated with MKE-to-EKE transfers) dominates globally and for the Gulf Stream, the Kuroshio, the Agulhas Current, and the Antarctic Circumpolar Current, whereas the secondary component (associated with EKE-to-MKE transfers) dominates for the Zapiola Gyre (Table 1).

2) PHYSICAL INTERPRETATION

Restarting from (17), we can rewrite the transfers in light of the Reynolds stress tensor (i.e., velocity covariance tensor) and its natural (i.e., eigenvalues and eigenvectors) decomposition:

$$
\begin{aligned}
&\{\mathrm{MKE} \leftrightarrow \mathrm{EKE}\}_{\mathrm{hor}} \\
&= \lambda_p(\hat{p}_x, \hat{p}_y)\begin{pmatrix} \overline{u'^2} & \overline{u'v'} \\ \overline{u'v'} & \overline{v'^2} \end{pmatrix}\begin{pmatrix} \hat{p}_x \\ \hat{p}_y \end{pmatrix} + \lambda_s(\hat{s}_x, \hat{s}_y)\begin{pmatrix} \overline{u'^2} & \overline{u'v'} \\ \overline{u'v'} & \overline{v'^2} \end{pmatrix}\begin{pmatrix} \hat{s}_x \\ \hat{s}_y \end{pmatrix}, \\
&= \lambda_p(\hat{p}_x, \hat{p}_y)\begin{pmatrix} \tilde{p}_x & \tilde{s}_x \\ \tilde{p}_y & \tilde{s}_y \end{pmatrix}\begin{pmatrix} \overline{u_p'^2} & 0 \\ 0 & \overline{u_s'^2} \end{pmatrix}\begin{pmatrix} \tilde{p}_x & \tilde{p}_y \\ \tilde{s}_x & \tilde{s}_y \end{pmatrix}\begin{pmatrix} \hat{p}_x \\ \hat{p}_y \end{pmatrix} \\
&\quad + \lambda_s(\hat{s}_x, \hat{s}_y)\begin{pmatrix} \tilde{p}_x & \tilde{s}_x \\ \tilde{p}_y & \tilde{s}_y \end{pmatrix}\begin{pmatrix} \overline{u_p'^2} & 0 \\ 0 & \overline{u_s'^2} \end{pmatrix}\begin{pmatrix} \tilde{p}_x & \tilde{p}_y \\ \tilde{s}_x & \tilde{s}_y \end{pmatrix}\begin{pmatrix} \hat{s}_x \\ \hat{s}_y \end{pmatrix}, \\
&= \lambda_p \overline{u_p'^2}(\hat{p}_x\tilde{p}_x + \hat{p}_y\tilde{p}_y)^2 + \lambda_p \overline{u_s'^2}(\hat{p}_x\tilde{s}_x + \hat{p}_y\tilde{s}_y)^2 \\
&\quad + \lambda_s \overline{u_p'^2}(\hat{s}_x\tilde{p}_x + \hat{s}_y\tilde{p}_y)^2 + \lambda_s \overline{u_s'^2}(\hat{s}_x\tilde{s}_x + \hat{s}_y\tilde{s}_y)^2, \qquad (18)
\end{aligned}
$$

where $(\tilde{p}_x, \tilde{p}_y)$ and $(\tilde{s}_x, \tilde{s}_y)$ are the eigenvectors associated with the eigenvalues $\overline{u_p'^2}$ and $\overline{u_s'^2}$, respectively, of the turbulent velocity covariance operator, so that $\tilde{p}_x\tilde{p}_x + \tilde{p}_y\tilde{p}_y = \tilde{s}_x\tilde{s}_x + \tilde{s}_y\tilde{s}_y = 1$ and $\tilde{p}_x\tilde{s}_x + \tilde{p}_y\tilde{s}_y = 0$. These directions are the empirical orthogonal function of the velocities, which maximize the velocity variance. This decomposition is often associated with the turbulence ellipsoid (Waterman and Lilly 2015). This shows that the transfers occur through the alignment of the natural directions of the Reynolds stress tensor with the natural directions of the mean flow deformation tensor (Fig. 10).

To shed light on the physical processes at play during the transfers, we consider the case where the horizontal transfers are the only process changing the horizontal velocities. Hence, after using (13) and rotating the framework along the natural directions of the mean flow deformation tensor, we obtain

$$
\begin{aligned}
&\partial_t\overline{\mathrm{EKE}} = \{\mathrm{MKE} \leftrightarrow \mathrm{EKE}\}_{\mathrm{hor}}, \\
&\overline{(u', v')\begin{pmatrix} \partial_t u' \\ \partial_t v' \end{pmatrix}} = \overline{(u', v')\begin{pmatrix} \hat{p}_x & \hat{s}_x \\ \hat{p}_y & \hat{s}_y \end{pmatrix}\begin{pmatrix} \lambda_p & 0 \\ 0 & \lambda_s \end{pmatrix}\begin{pmatrix} \hat{p}_x & \hat{p}_y \\ \hat{s}_x & \hat{s}_y \end{pmatrix}\begin{pmatrix} u' \\ v' \end{pmatrix}}.
\end{aligned}
$$

Since this equation directly derives from (4a) and (4b), we can write explicitly the contribution from zonal and meridional velocities:

$$
\begin{aligned}
&\begin{pmatrix} \partial_t u' \\ \partial_t v' \end{pmatrix} = \begin{pmatrix} \hat{p}_x & \hat{s}_x \\ \hat{p}_y & \hat{s}_y \end{pmatrix}\begin{pmatrix} \lambda_p & 0 \\ 0 & \lambda_s \end{pmatrix}\begin{pmatrix} \hat{p}_x & \hat{p}_y \\ \hat{s}_x & \hat{s}_y \end{pmatrix}\begin{pmatrix} u' \\ v' \end{pmatrix}, \\
&\begin{cases} \partial_t \hat{u}' = \dfrac{1}{2}(-\Delta + \sigma)\hat{u}', \\ \partial_t \hat{v}' = \dfrac{1}{2}(-\Delta - \sigma)\hat{v}', \end{cases} \qquad (19)
\end{aligned}
$$

where $(\hat{u}' = \hat{p}_x u' + \hat{p}_y v')$ and $(\hat{v}' = \hat{s}_x u' + \hat{s}_y v')$ are the velocity anomalies aligned to the primary and secondary natural directions of the mean flow deformation tensor, respectively. These expressions suggest the existence of instability and stability directions where anomalous velocities grow or decay, respectively. Physically, this corresponds to the extraction from the mean flow (or mean velocity gradient) of momentum by the anomalous velocity. This quantitative derivation and

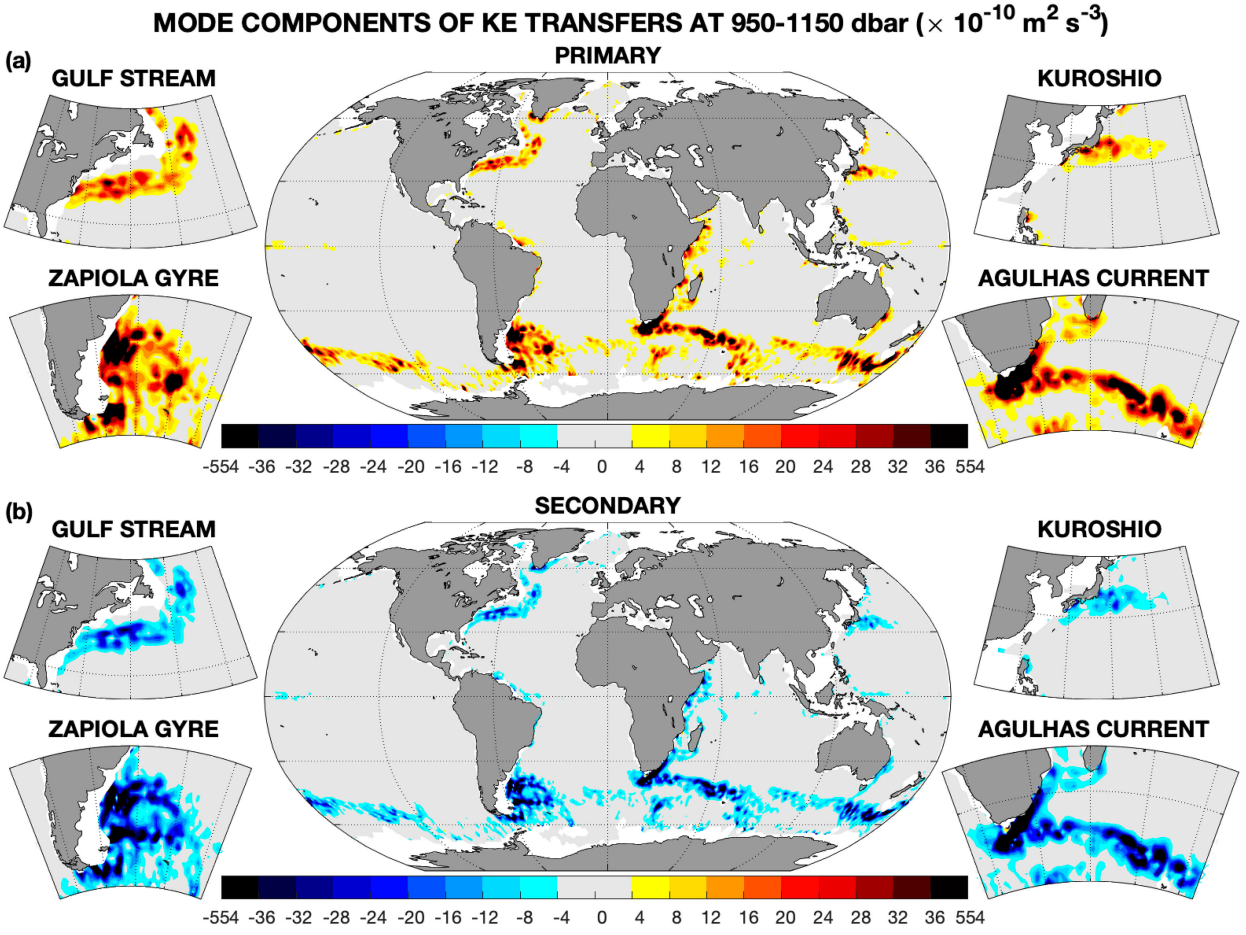

FIG. 9. Modes of horizontal transfers of KE from MKE to EKE. As in Fig. 4, but for each of the KE transfer components of the decomposition (17), based on mean flow properties: (a) primary and (b) secondary mode components. Positive and negative values show MKE-to-EKE and EKE-to-MKE transfers, respectively. Insets (clockwise from top left) show magnification for the Gulf Stream, Kuroshio, Agulhas Current, and Zapiola Gyre regions.

analytical result are consistent with the qualitative description of Kundu (1990) about the intensification and decay of eddies along the primary and secondary strain directions. Three cases occur: 1) If $|\Delta| < \sigma$, there is one unstable direction and one stable direction (saddle point); 2) if $|\Delta| > \sigma$ and $\Delta > 0$, the two directions are stable (stable node); and 3) if $|\Delta| > \sigma$ and $\Delta < 0$, the two directions are unstable (unstable node). [$|\Delta| = \sigma$ being a degenerate case falling in the category (1), but with one direction being neutral and one direction being either stable or unstable depending if $\Delta \lessgtr 0$.] This growth or decay of velocity perturbation can be interpreted as a growth or decay of EKE. Hence, in the context of KE transfers, this suggests MKE-to-EKE and EKE-to-MKE transfers, respectively. Since the flow is mainly strain dominated (Fig. 8), case (1) appears to be more typical, suggesting the coexistence of two orthogonal directions, one corresponding to MKE-to-EKE transfers and the other to EKE-to-MKE transfers.

To illustrate this mechanism and the induced KE transfers, we look in detail to the velocity field between 50° and 30°S and between 45° and 75°E, a region of the Antarctic Circumpolar Current downstream of the Agulhas Current, near the Kerguelen Plateau. At this location, the MKE reached up to 280 $cm^2\ s^{-2}$ (i.e., ~17 $cm\ s^{-1}$ of velocity magnitude), whereas the EKE reached up to 400 $cm^2\ s^{-2}$ (Figs. 11a,b, respectively). The mean flow shows a well-defined jet. We interpret the KE transfers through (18), setting the framework of natural directions of the mean flow deformation and of the velocity covariance described in (Fig. 10). The computation of the eigenvectors of the mean flow deformation tensor corresponds to a positive direction along the southwest/northeast direction north of the jet and along the southeast/northwest direction south of the jet (the negative direction being orthogonal by construction). This rotation of the natural direction is expected for a jet (since the gradient flips sign across the flow direction). The gradients are stronger at the edge of the jet and are primarily controlled by the strain rather than the divergence. On the other hand, the EKE is intensified close to the core of the jet. It shows a prevailing zonal direction, mainly aligned with the jet. The resulting transfers occur north and south of the jet

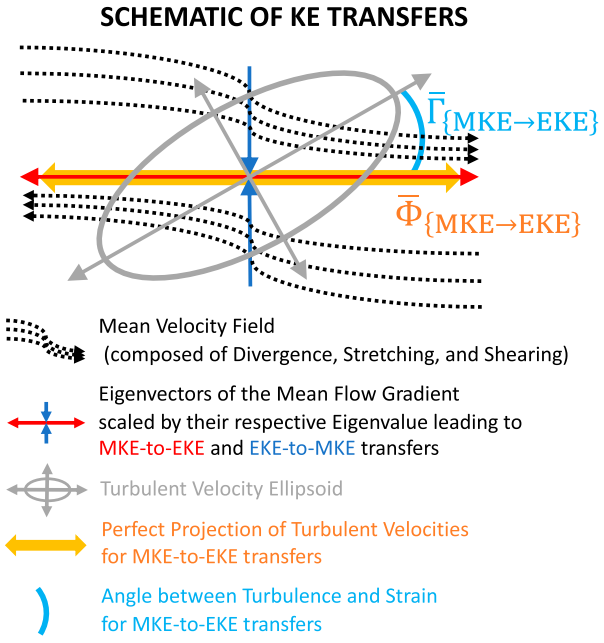

FIG. 10. Schematic of the KE transfers. The schematic represents the KE transfers induced by the local eddy–mean interactions. The mean flow (black dotted arrows) can be represented through the eigenvectors of the mean flow deformation tensor (controlled by its shearing, stretching, and divergence) scaled by their respective eigenvalues (controlled by its strain and divergence), leading to the direction of MKE-to-EKE and EKE-to-MKE transfers (red and blue arrows, respectively). The turbulence is represented by the velocity variance ellipsoid representative of the Reynolds stress (gray arrows and ellipsoid). Here, two diagnostics summarizing the KE transfers are represented. The transfer potential from MKE to EKE ($\overline{\Phi}_{\{MKE\rightarrow EKE\}}$—orange double arrow) corresponds to the assumed perfect projection of the turbulence on the direction of the mean flow gradient eigenvectors. The transfer efficiency from MKE to EKE ($\overline{\Gamma}_{\{MKE\rightarrow EKE\}}$—cyan arc) measures the angle between the turbulence and the mean flow deformation.

(Fig. 11c), with MKE to EKE and EKE to MKE located north and south of the jet, respectively. This is consistent with the 90° rotation of the natural direction of the mean flow deformation tensor from the north to the south of the jet (colors vs red and blue crosses in Fig. 11c), further confirming the control of the KE transfers by the mean flow strain. The transfers correspond to decelerating and accelerating the mean jet and to increasing and decreasing the eddy turbulence north and south of the jet, respectively. This leads to a southward shift of MKE and a northward shift of EKE, creating a latitudinal offset between MKE and EKE (Fig. 11d).

It is worth noting that, in this particular region where the flow is quite zonal allowing for a coordinate-dependent decomposition, the anisotropic component (and the covariance one, to some extent) obtained with the physical turbulent decomposition also exhibits positive and negative KE transfers south and north of the jet, respectively (Figs. 6c,d). This demonstrates the usefulness and consistency of the two interpretations/decompositions.

3) DIAGNOSTICS

As demonstrated above, the amplitude of turbulent velocities (measured by the EKE) and the amplitude of the mean flow deformation (measured by λ_p and λ_s) will play a role in the amplitude of the kinetic energy transfers. Hence, we can define the potential of kinetic energy transfers. This could be expressed as the transfer values achieved if the turbulent flow is perfectly aligned to the primary or secondary directions of the mean flow deformation (Fig. 10). This reads

$$\overline{\Phi}_{\{MKE\rightarrow EKE\}} = \lambda_p(\overline{u'^2} + \overline{v'^2}), \tag{20a}$$

$$\overline{\Phi}_{\{EKE\rightarrow MKE\}} = \lambda_s(\overline{u'^2} + \overline{v'^2}). \tag{20b}$$

These indices can also be defined instantaneously as $\Phi_{\{MKE\rightarrow EKE\}}(t) = \lambda_p(u'^2 + v'^2)$ and $\Phi_{\{EKE\rightarrow MKE\}}(t) = \lambda_s(u'^2 + v'^2)$. The dominance of one transfer potential over the other can only come from the dominance of one eigenvalue over the other. As expressed in (16), this can only occur through the existence of horizontal divergence of the mean flow (and not the strain magnitude of the flow).

The overall pattern of the potential of the primary and secondary components is close to their components themselves (Fig. 12), with high amplitude in intense western boundary currents and in the Southern Ocean. However, the computed potentials are of magnitude significantly higher than their actual values. This means that the KE transfers for both MKE to EKE and EKE to MKE can be more important than the actual transfers. Also, we find that the potential of the primary component (associated with MKE-to-EKE transfers) is higher than the potential of the secondary component (associated with EKE-to-MKE transfers) both globally and for all tested regions (Table 1). This suggests that the deep ocean is indeed more prone to MKE-to-EKE transfers. These properties are directly derived from the divergence of the mean horizontal flow (as discussed above for the eigenvalues). Also, this consistency further confirms the usefulness of the decomposition through the natural properties of the mean flow.

Besides the potential of the transfers, the more the turbulent velocity is aligned to the primary or secondary direction, the more efficient the transfers from MKE to EKE or EKE to MKE are (Fig. 10). For the MKE-to-EKE transfers, this efficiency term can be measured by the normalized projection of the turbulence onto the primary direction as

$$\overline{\Gamma}_{\{MKE\rightarrow EKE\}} = \overline{\left[\frac{(u'\hat{p}_x + v'\hat{p}_y)^2}{u'^2 + v'^2}\right]}; \tag{21a}$$

whereas, it is

$$\overline{\Gamma}_{\{EKE\rightarrow MKE\}} = \overline{\left[\frac{(u'\hat{s}_x + v'\hat{s}_y)^2}{u'^2 + v'^2}\right]}, \tag{21b}$$

for the efficiency of EKE-to-MKE transfers. The numerator is the covariance of the turbulence with the natural directions of

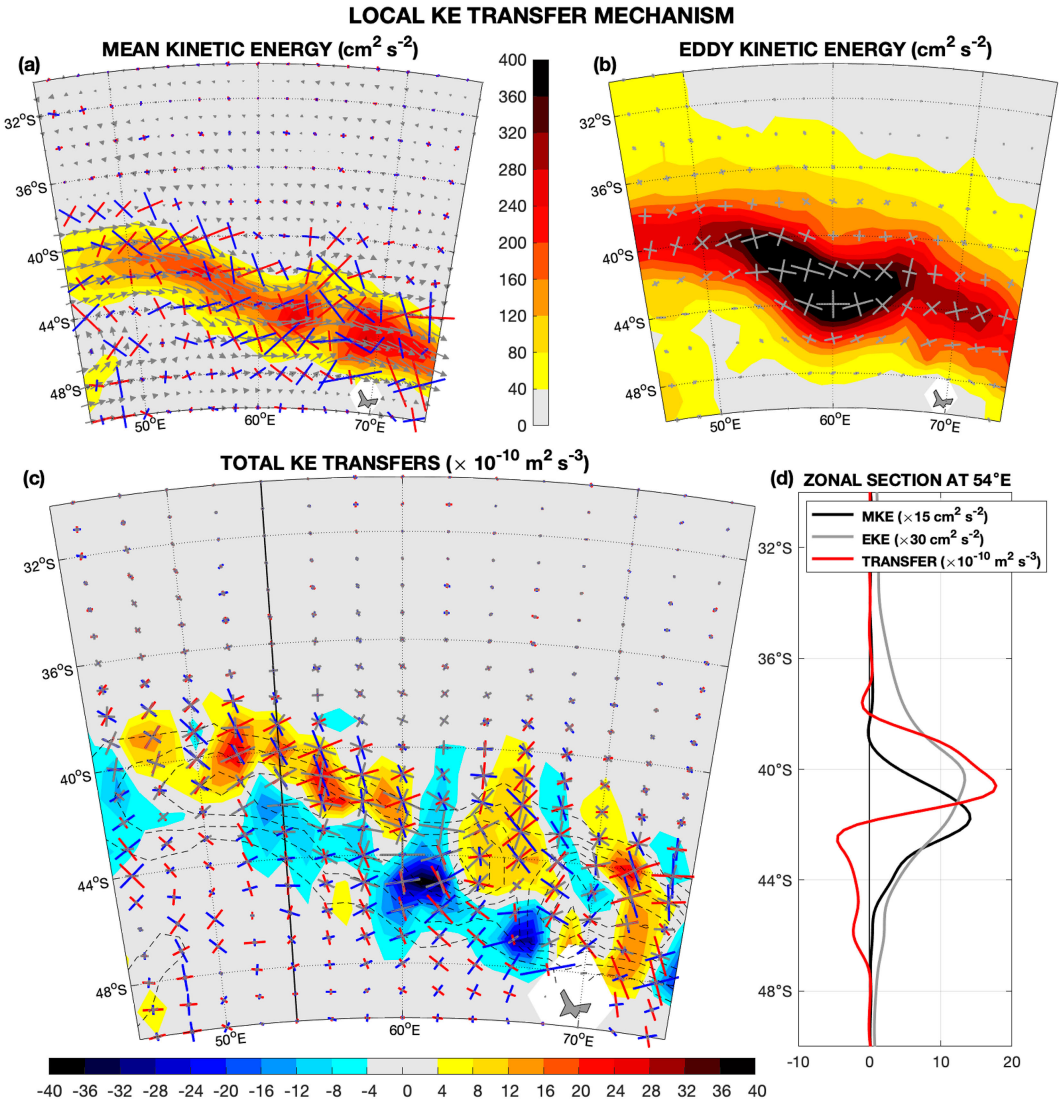

FIG. 11. Local example of KE transfers. ACC downstream of the Agulhas Current, near the Kerguelen Plateau. (a) MKE (color shading), horizontal mean velocities (gray arrows), and the primary and secondary directions multiplied by their respective amplitude (crosses) show the direction of MKE-to-EKE and EKE-to-MKE transfers (through the red and blue segments), respectively, and are set by the natural directions of the mean flow deformation tensor (or mean strain tensor). (b) EKE (color shading) and the respective primary and secondary directions of the turbulence (gray crosses) representing the turbulence ellipsoid and set by the natural directions of the velocity covariance tensor (or Reynolds stress tensor). (c) The total kinetic transfers (color shading), the MKE (dashed contours from 0 with a contour interval of 40 cm^2 s^{-2}), the natural turbulent directions (gray crosses), and the natural directions of the mean flow deformation tensor (colored crosses). Positive and negative values show MKE-to-EKE and EKE-to-MKE transfers, respectively. (d) Meridional section at 54°E indicated by the thin black line in (c) with spline interpolation on a regular 0.01° grid.

the mean flow deformation tensor (corresponding to the strain directions). Note that the denominator is simply the EKE and that these indices could be defined instantaneously such as $\Gamma_{\{\mathrm{MKE}\to\mathrm{EKE}\}}(t) = (u'\hat{p}_x + v'\hat{p}_y)^2/(u'^2 + v'^2)$ and $\Gamma_{\{\mathrm{EKE}\to\mathrm{MKE}\}}(t) = (u'\hat{s}_x + v'\hat{s}_y)^2/(u'^2 + v'^2)$. It is also worth noting that since the eigenvectors $(\hat{p}_x, \hat{p}_y)$ and $(\hat{s}_x, \hat{s}_y)$ defined an orthogonal basis, the sum of the efficiency terms is 1. So that the efficiency indices measure which of the two pathways is preferred: either MKE to EKE or EKE to MKE, since $\overline{\Gamma}_{\{\mathrm{MKE}\to\mathrm{EKE}\}} + \overline{\Gamma}_{\{\mathrm{EKE}\to\mathrm{MKE}\}} = 1$, by construction.

The efficiency reveals a small-scale dominant geographical pattern, with values further away from balance (i.e., 0.5) in the equatorial band (Fig. 13a). The statistical distribution is quite tight and centered around 0.5 (Fig. 13b). Spatial averages also show that the efficiencies of MKE to EKE and EKE to MKE are equivalent (Table 1). This means that the

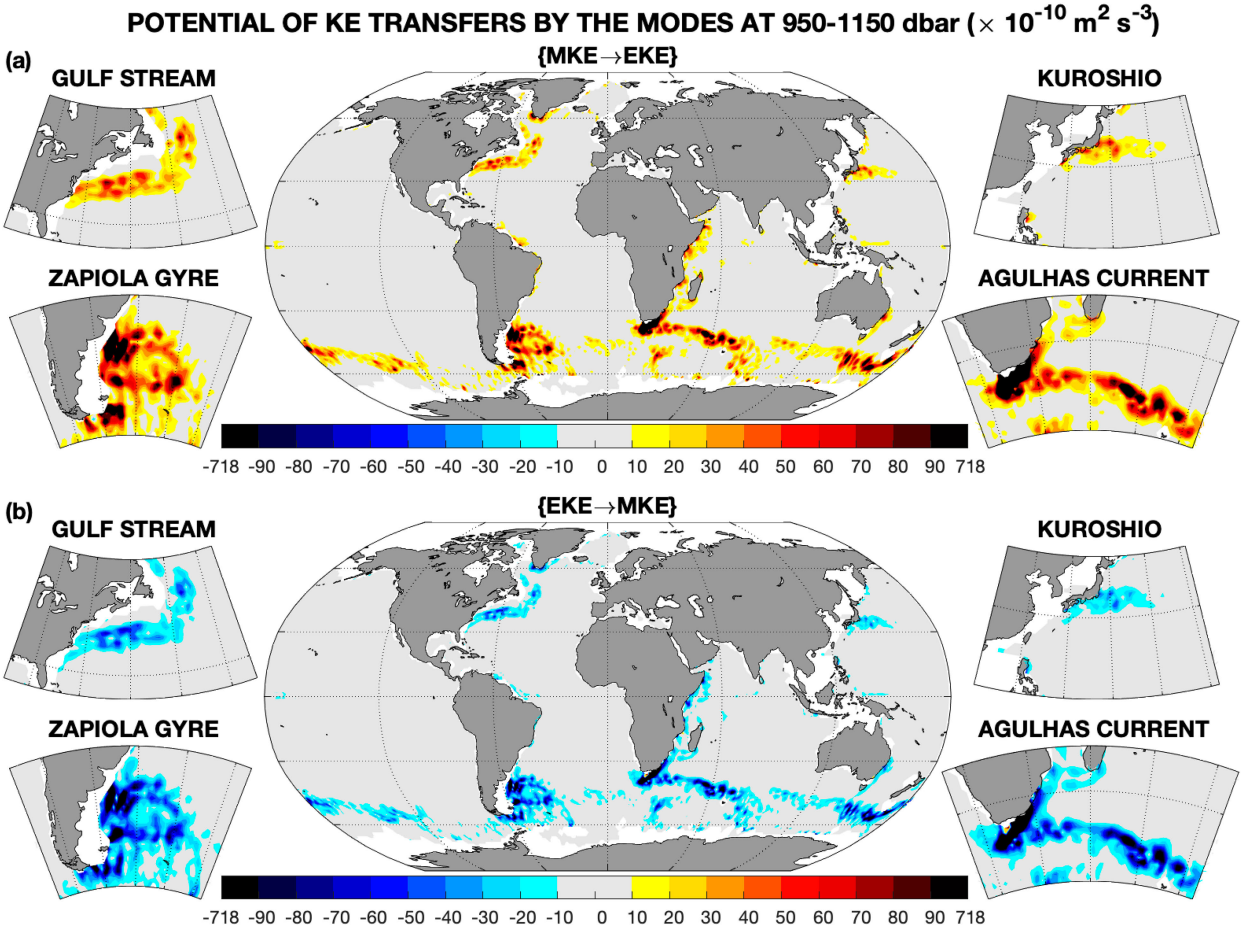

FIG. 12. Potential of MKE-to-EKE and EKE-to-MKE transfers. (a) Potential of MKE-to-EKE transfers ($\overline{\Phi}_{\{MKE\to EKE\}}$) and (b) potential of EKE-to-MKE transfers ($\overline{\Phi}_{\{EKE\to MKE\}}$), following (20). Positive and negative values show MKE-to-EKE and EKE-to-MKE transfers, respectively. Insets (clockwise from top left) show magnification for the Gulf Stream, Kuroshio, Agulhas Current, and Zapiola Gyre regions.

direction of the turbulent flow is well balanced between the primary and secondary directions of the mean flow deformation tensor both globally and for the Gulf Stream, the Kuroshio, the Agulhas Current, and the Antarctic Circumpolar Current. Hence, in these regions, the turbulence does not favor specifically MKE-to-EKE transfers or EKE-to-MKE transfers. This leaves the dominance of the transfers to their respective potentials (controlled by the horizontal mean flow), which favored MKE-to-EKE transfers in all tested regions and globally (through the horizontal mean flow divergence). On the other hand, the turbulence slightly favored EKE-to-MKE transfers for the Zapiola Gyre ($\overline{\Gamma}_{\{MKE\to EKE\}}$ is equal to 0.49 when averaged over this region). This small increase in the efficiency of EKE-to-MKE transfers leads to net EKE-to-MKE transfers, despite the dominance of the MKE-to-EKE transfer potential. Hence, there, and unlike other tested regions, the turbulence is able to dictate the direction of the KE transfers, despite the mean flow preference, making the Zapiola Gyre a quite unique region.

5. Discussion and conclusions

Changes and variability in the ocean are seen on a large range of time scales (Dijkstra 2000). Intense large-scale mean currents are often also associated with intense mesoscale eddy-driven turbulence. This raises questions about the interactions between mean and eddy flow, in particular on the transfer of kinetic energy between the mean kinetic energy, associated with the mean flow, and the eddy kinetic energy, associated with the mesoscale eddy turbulence and submesoscale processes.

In this study, we have used deep Argo float displacements centered around 1000-m depth to estimate the horizontal transfers of kinetic energy between the mean kinetic energy and the eddy kinetic energy (section 4). We show that these transfers occur mainly in the Southern Ocean and in the vicinity of western boundaries, especially in energetic regions such as the Gulf Stream, the Kuroshio, the Zapiola Gyre, the Agulhas Current, and the Antarctic Circumpolar Current (Fig. 4). We show that the geographical patterns of these transfers are small-scale dominant and that their spatial averages are small residuals of intense local values. The MKE-to-EKE transfer is

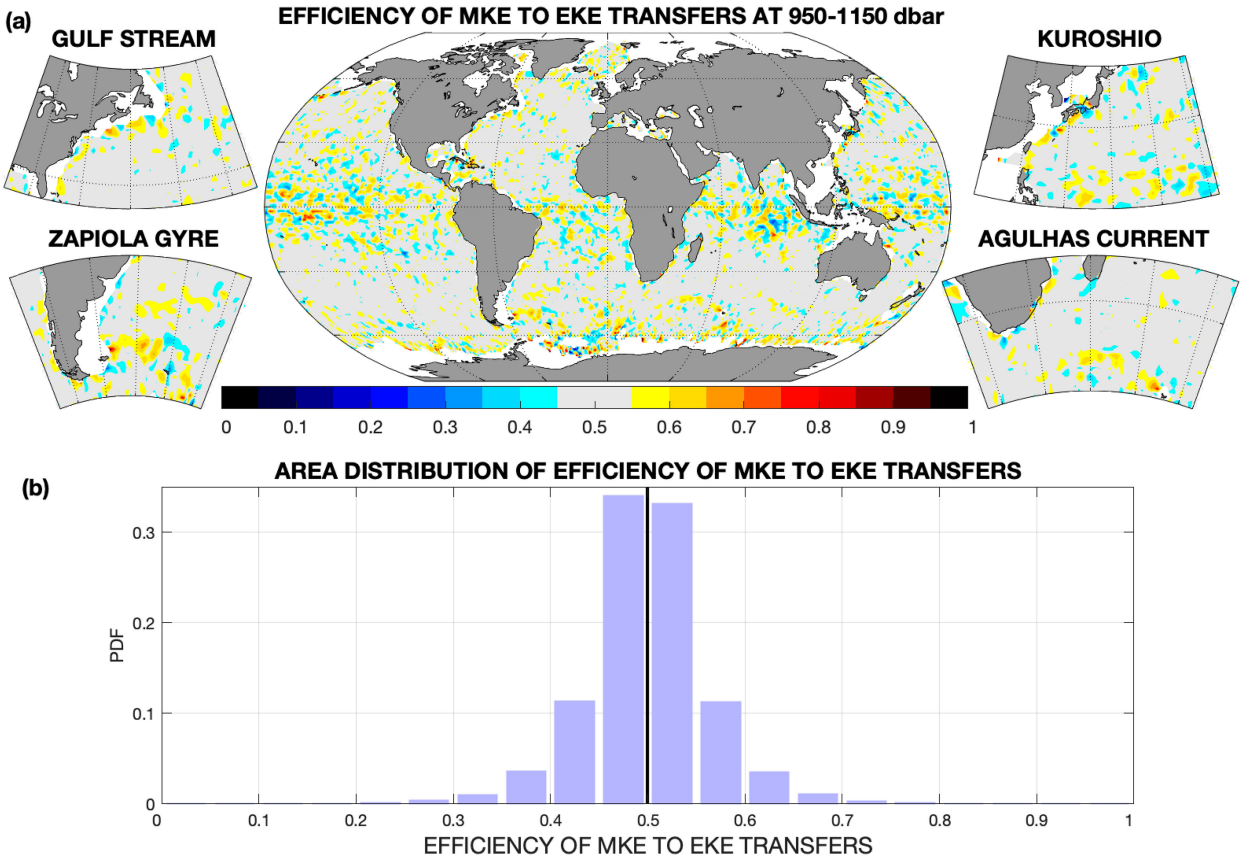

FIG. 13. Efficiency of MKE-to-EKE transfers. (a) Geographical map and (b) distribution of the efficiency of MKE-to-EKE transfers ($\overline{\Gamma}_{\{MKE\to EKE\}}$), respectively, following (21a). Values above or below 0.5 show regions more favorable to MKE-to-EKE or EKE-to-MKE transfers, respectively. Value 0 or 1 shows region purely following EKE-to-MKE or MKE-to-EKE transfers, respectively. Insets in (a) (clockwise from top left) show magnification for the Gulf Stream, Kuroshio, Agulhas Current, and Zapiola Gyre regions.

favored globally and in regional averages of the Gulf Stream, the Kuroshio, the Agulhas Current, and the Antarctic Circumpolar Current regions (Table 1). However, the Zapiola region appears to be a unique region where an EKE-to-MKE transfer is favored. This is consistent with theoretical and numerical studies (e.g., de Miranda et al. 1999), but it is the first time that this transfer is observed experimentally.

We have tested two decompositions, one that follows the physical properties of the turbulent flow (isotropic, anisotropic, and covariance; section 4b) and one that follows the natural properties of the mean flow (i.e., eigenvectors of the mean flow deformation tensor; section 4c). The former does not appear to be extremely useful to better understand the essence of KE transfers. Indeed, the physical decomposition suffers from a coordinate dependency. This is not always problematic, such as in an idealized setting (e.g., zonally periodic configurations) or in the atmosphere (where the circulation is more zonal), but this is an issue in the ocean (where the mean flow is less consistently aligned). This difficulty is overcome by the decomposition using the natural mean flow properties for which amplitude components are coordinate invariant (i.e., composed of the divergence and strain magnitude). We conclude that the decomposition using natural mean flow properties is thus more robust for analyzing real ocean observations. Hence, this decomposition, equivalent to a dynamical attribution, allows us to demonstrate the unique existence of two transfer modes: one from MKE to EKE and one from EKE to MKE. These two modes are significantly more intense than their sum (Fig. 9), suggesting that actual KE transfers are small residuals of two competing effects. These two effects depend on whether the horizontal strain acts constructively with or opposes the effect of the horizontal divergence.

The physical decomposition of the turbulence follows Hoskins et al. (1983), which has been shown to be useful for understanding the momentum forcing by the turbulence (Waterman and Hoskins 2013; Waterman and Lilly 2015). However, here, in the context of KE transfers, with both turbulence and mean flow deformation contributing, it appears less useful to decompose the turbulence than the mean flow deformation (Fig. 6 vs Fig. 9). However, these two decompositions remain related since the projection of the turbulence (and so of its natural directions, defining the turbulence ellipsoid, as discussed in Waterman and Lilly 2015) onto the natural directions of mean flow gradients (mainly corresponding to the strain directions) sets the KE transfers (Fig. 10). This is visible in our key equations [(17) and

(18)] describing the decomposition of KE transfers. We rationalized the usefulness of the natural decomposition of the mean flow, over the physical decomposition of the turbulence, due to the fact that KE transfers derive from momentum instabilities, that are ultimately controlled by the mean momentum gradients. Hence, the natural decomposition of the mean flow can be physically interpreted through the classical framework of eddy growth/decay (Kundu 1990).

The decomposition using the natural properties of the mean flow deformation allows to develop two diagnostics [section 4c(3)]. One measures the potential of MKE-to-EKE transfers and of EKE-to-MKE transfers and the other measures the respective efficiency of these two transfers. The former shows the maximum intensity that can be reached by the transfers if the turbulence is optimally aligned with the mean flow deformation. The latter shows how the turbulence is aligned with mean flow deformation. Hence, efficiency is a measure of which transfer direction is favored. Application of the potential diagnostics reveals that the MKE-to-EKE potential always dominates over the EKE-to-MKE potential for all tested regions and globally. Regarding efficiency, this diagnostic suggests that the two transfer directions are well balanced in most tested regions (Gulf Stream, Kuroshio, Agulhas Current, and Antarctic Circumpolar Current) and globally. However, when averaged over the Zapiola Gyre, the efficiency suggests a slight unbalance in favor of the EKE-to-MKE transfer. This makes the Zapiola Gyre a unique location, where the turbulent dynamics favor EKE-to-MKE transfer.

Our analysis suggests that the KE transfers are better rationalized by the mean flow properties (rather than by the turbulent flow properties). Also, despite being a scalar, our natural decomposition explicitly distinguishes between the directions of KE transfers [(19)], making it well suited for a generalization to a momentum directional parameterization. This shows the potential to develop a small-scale closure available for the large-scale flow. This potential is further confirmed by the computation of the efficiency of the transfers, which shows that the direction of the turbulent flow is not particularly aligned to the natural direction of the flow at the global scale and for the Gulf Stream, Kuroshio, Agulhas Current, and Antarctic Circumpolar Current regions. This conclusion is not robust for the Zapiola Gyre region and at the local scale. Nonetheless, we have provided a method and a map to determine such direction that can be incorporated into a small-scale closure.

An alternative interpretation of EKE is the variance of small-scale velocity amplitude. Hence, the prevailing direction of KE transfers controls the variance growth and MKE-to-EKE or EKE-to-MKE transfers can be reinterpreted as source or sink of small-scale variance. This makes this diagnostic well suited to discuss small-scale predictability. In this framework, we find that regions of intense ocean dynamics, such as the western boundaries and the Southern Ocean, exhibit significant growth of small-scale variance. At a regional scale, the Gulf Stream, Kuroshio, Agulhas Current, and Antarctic Circumpolar Current exhibit variance growth on average, unlike the Zapiola Gyre. At the global scale, our diagnostic also suggests the growth of small-scale variance.

Following the same principle, we now focus on the relevance of our results for the large-scale momentum magnitude (measured by the MKE). Since the length of the dataset is a bit shorter than two decades, this allows us to assess the role of turbulence on this two-decade "mean" climate. We find that the turbulence slows down the flow magnitude on average (i.e., MKE-to-EKE transfer is positive). At a regional scale, we find this result to be consistent for energetic regions such as the Gulf Stream, the Kuroshio, the Agulhas Current, and the Antarctic Circumpolar Current. However, the region of the Zapiola Gyre exhibits positive transfers from the turbulence to the magnitude of the flow, suggesting that the turbulence accelerates the mean circulation (as shown in numerical models by de Miranda et al. 1999). Also, on a local level, there exist numerous regions where the mean flow magnitude is accelerated by the turbulence. Hence, we conclude that the turbulence can accelerate the mean flow locally but slow down the circulation on a larger scale (i.e., global mean or large tested regions, except for the Zapiola Gyre).

We have also shown that the mean velocity gradient tensor is similar to the Jacobian matrix for tracer gradient dynamics (Okubo 1970; Weiss 1991). This is arguably the result which offers the most interesting perspective. In particular, we find that the eigenvalue decomposition of the mean flow deformation tensor leads to the exact same solution as the decomposition for tracer gradient magnitude (Balwada et al. 2021). This demonstrates that gradient growth or decay is associated with kinetic energy transfers from MKE to EKE or EKE to MKE, respectively. This will be the topic of future investigations.

Our analysis suffers from inherent shortcomings. One key issue of the dataset is the possible spurious divergence of the mean flow, mainly because of the averaging of trajectories occurring at different times and spaces. Despite not being the dominant term over the strain magnitude (Figs. 3 and 8), we have tested a different dataset to define the mean (Ollitrault and Colin de Verdière 2014; Colin de Verdière et al. 2019). The computation of KE transfers with this dataset, that constrains the flow to be fully geostrophic (restricting the divergence), does not show significant qualitative or quantitative differences.

As with any observation, the ANDRO dataset cannot sample the full continuous range of ocean processes. We have tested the convergence of the results by subsampling the dataset (using previous less-complete official releases). This test shows the overall excellent convergence of the KE transfers and of the suggested decompositions and diagnostics. However, this does not test if a key scale is still not sampled (e.g., small-scale permanent front—rarely visited by Argo floats during their journey at depth). To build confidence on the robustness of our analysis, we could compare the overall KE transfers with those of independent analyses (including mooring measurements, state estimates, and numerical models), which do not suffer from this particular sample issue. Phillips and Rintoul (2000) found values of KE transfers $(1.6 \pm 9.4) \times 10^{-9}$ m^2 s^{-3} at 11 500 dbar using mooring observations of Drake Passage, consistent with our evaluations. Chen et al. (2014b) found the same key locations in KE transfers as we

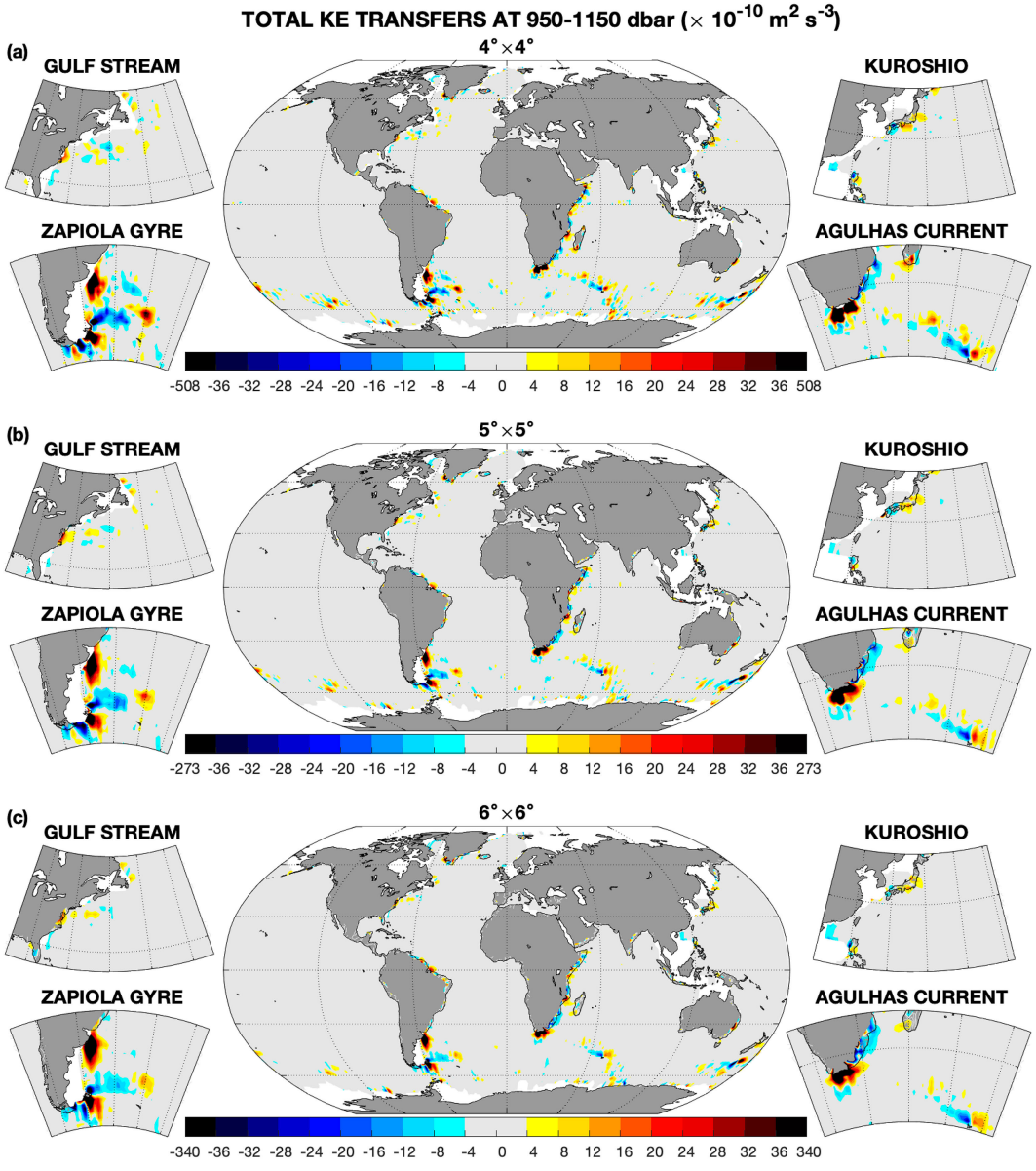

FIG. 14. Sensitivity of total MKE-to-EKE transfers to gridcell size. As in Fig. 4, but for flow statistics computed using (a) 4° × 4°, (b) 5° × 5°, and (c) 6° × 6°cells.

do in both altimetry reconstruction and state estimate for surface transfers, but with a larger amplitude ($\pm 10^{-8}$ m^2 s^{-3}), as expected for surface values compared to 1000-m deep ones. In a high-resolution state estimate, Zhu et al. (2018) show the existence of a positive intensification of KE transfers at the south of the tip of South Africa consistent with our results. Their typical values are $\pm 10^{-6}$ m^2 s^{-3} for the upper 500 m in the Agulhas Current region. These values are above ours, but still in the expected range given the different depths. In high-resolution models, Kang and Curchitser (2015) and Yan et al. (2019) obtained values of KE transfers at 1000-m depth of $\pm 10^{-8}$ m^2 s^{-3} in the Gulf Stream region and of 5×10^{-8} m^2 s^{-3} in the Kuroshio region, respectively. All these previous studies have obtained geographical patterns and amplitudes consistent with our estimates.

Given the spatiotemporal average used in our study, the interpretation of KE transfers has to be done with care. One possible interpretation is to consider the average as a temporal average where observations are considered consistent over the spatial scale of the grid. From (14), we have two actions of the grid size on the KE transfers. The first is the scale selection needed to define MKE and EKE reservoirs, setting both turbulent velocities and the properties of the mean flow deformation tensor. The second is a smoothing of the overall KE transfers (as depicted by the large overbar on the right-hand side of the equation). Following this idea, we have tested a

range of grid sizes from 3° × 3° to 6° × 6°. This shows that our results are robust, beyond the typical smoothing expected with the use of wider grids (Fig. 14).

Our results focusing on large-scale average for the mean state are aligned with the dynamics of coarse, laminar ocean models that still remain currently routinely used for climate projections. Nevertheless, it is highly possible that KE transfers acting at a smaller scale are even more intense than the ones described in the present study because strain magnitude is higher at mesoscales and submesoscales. Refining our results for smaller scales is a direction for future work.

Beyond that, the most obvious shortcoming is the single-depth approach constrained by the depth of Argo float deep displacements. It would be interesting to generalize our results and analysis to other depths. However, this approach might be restricted to a numerical approach since in situ observations at all depths do not exist. On the other hand, since there are observations by surface Lagrangian buoys, another direction for future work will be to specifically target the surface. There, other processes contribute to the horizontal displacements (e.g., Ekman transport or surface wave Stokes drift). Hence, we would like to estimate how these new processes modify the suggested picture of deep KE transfers. This might be directly (through momentum transfers) or indirectly (through heat transfers) important for the impact of the ocean on the atmosphere and, hence, on the climate and its predictability.

Acknowledgments. This research was supported by the ARVOR project funded through the French CNRS/INSU/LEFE program, by the OceaniX project funded through the French ANR program, and by the ISblue project, the Interdisciplinary Graduate School for the Blue Planet (ANR-17-EURE-0015), and cofunded by a grant from the French government under the program "Investissements d'Avenir." The ANDRO Argo float displacement product is made freely available by SNO Argo France at LOPS Laboratory (supported by UBO/CNRS/Ifremer/IRD) and IUEM Observatory (OSU IUEM/CNRS/INSU) and was funded by Ifremer, Coriolis, SOERE-CTDO2, and SNO Argo France.

Data availability statement. The ANDRO dataset used in this study corresponds to the 2022 release (key: "91950") and is freely available through the www.seanoe.org platform (https://doi.org/10.17882/47077).

REFERENCES

Arbic, B. K., M. Müller, J. G. Richman, J. F. Shriver, A. J. Morten, R. B. Scott, G. Sérazin, and T. Penduff, 2014: Geostrophic turbulence in the frequency–wavenumber domain: Eddy-driven low-frequency variability. *J. Phys. Oceanogr.*, **44**, 2050–2069, https://doi.org/10.1175/JPO-D-13-054.1.

Balwada, D., Q. Xiao, S. Smith, R. Abernathey, and A. R. Gray, 2021: Vertical fluxes conditioned on vorticity and strain reveal submesoscale ventilation. *J. Phys. Oceanogr.*, **51**, 2883–2901, https://doi.org/10.1175/JPO-D-21-0016.1.

Brandt, P., A. Funk, V. Hormann, M. Dengler, R. J. Greatbatch, and J. M. Toole, 2011: Interannual atmospheric variability forced by the deep equatorial Atlantic Ocean. *Nature*, **473**, 497–500, https://doi.org/10.1038/nature10013.

Chelton, D. B., M. G. Schlax, R. M. Samelson, and R. A. de Szoeke, 2007: Global observations of large oceanic eddies. *Geophys. Res. Lett.*, **34**, L15606, https://doi.org/10.1029/2007GL030812.

Chen, R., G. R. Flierl, and C. Wunsch, 2014a: A description of local and nonlocal eddy–mean flow interaction in a global eddy-permitting state estimate. *J. Phys. Oceanogr.*, **44**, 2336–2352, https://doi.org/10.1175/JPO-D-14-0009.1.

——, J. L. McClean, S. T. Gille, and A. Griesel, 2014b: Isopycnal eddy diffusivities and critical layers in the Kuroshio extension from an eddying ocean model. *J. Phys. Oceanogr.*, **44**, 2191–2211, https://doi.org/10.1175/JPO-D-13-0258.1.

——, A. F. Thompson, and G. R. Flierl, 2016: Time-dependent eddy-mean energy diagrams and their application to the ocean. *J. Phys. Oceanogr.*, **46**, 2827–2850, https://doi.org/10.1175/JPO-D-16-0012.1.

Colin de Verdière, A., 1979: Mean flow generation by topographic Rossby waves. *J. Fluid Mech.*, **94**, 39–64, https://doi.org/10.1017/S0022112079000938.

——, and M. Ollitrault, 2016: A direct determination of the World Ocean barotropic circulation. *J. Phys. Oceanogr.*, **46**, 255–273, https://doi.org/10.1175/JPO-D-15-0046.1.

——, T. Meunier, and M. Ollitrault, 2019: Meridional overturning and heat transport from Argo floats displacements and the planetary geostrophic method: Applications to the subpolar North Atlantic. *J. Geophys. Res. Oceans*, **124**, 6270–6285, https://doi.org/10.1029/2018JC014565.

Davidson, P. A., 2004: *Turbulence: An Introduction for Scientists and Engineers*. Oxford University Press, 657 pp.

Davis, R. E., 1991: Observing the general circulation with floats. *Deep-Sea Res.*, **38A** (Suppl.), S531–S571, https://doi.org/10.1016/S0198-0149(12)80023-9.

Delpech, A., S. Cravatte, F. Marin, C. Ménesguen, and Y. Morel, 2020: Deep eddy kinetic energy in the tropical Pacific from Lagrangian floats. *J. Geophys. Res. Oceans*, **125**, e2020JC016313, https://doi.org/10.1029/2020JC016313.

de Miranda, A. P., B. Barnier, and W. K. Dewar, 1999: On the dynamics of the Zapiola Anticyclone. *J. Geophys. Res.*, **104**, 21 137–21 149, https://doi.org/10.1029/1999JC900042.

Dewar, W. K., 1998: Topography and barotropic transport control by bottom friction. *J. Mar. Res.*, **56**, 295–328, https://doi.org/10.1357/002224098321822320.

Dijkstra, H. A., 2000: *Nonlinear Physical Oceanography*. Springer, 456 pp.

Farrell, B. F., and P. J. Ioannou, 1996a: Generalized stability theory. Part I: Autonomous operators. *J. Atmos. Sci.*, **53**, 2025–2040, https://doi.org/10.1175/1520-0469(1996)053<2025:GSTPIA>2.0.CO;2.

——, and ——, 1996b: Generalized stability theory. Part II: Nonautonomous operators. *J. Atmos. Sci.*, **53**, 2041–2053, https://doi.org/10.1175/1520-0469(1996)053<2041:GSTPIN>2.0.CO;2.

Ferrari, R., and C. Wunsch, 2009: Ocean circulation kinetic energy: Reservoirs, sources, and sinks. *Annu. Rev. Fluid Mech.*, **41**, 253–282, https://doi.org/10.1146/annurev.fluid.40.111406.102139.

Freeland, H. J., P. B. Rhines, and T. Rossby, 1975: Statistical observations of trajectories of neutrally buoyant floats in the North Atlantic. *J. Mar. Res.*, **33**, 383–404.

Gille, S. T., 2003: Floats observations of the Southern Ocean. Part II: Eddy fluxes. *J. Phys. Oceanogr.*, **33**, 1182–1196, https://doi.org/10.1175/1520-0485(2003)033<1182:FOOTSO>2.0.CO;2.

Hall, M. M., 1986: Assessing the energetics and dynamics of the Gulf Stream at 68W from moored current measurements. *J. Mar. Res.*, **44**, 423–443.

Harrison, D. E., and A. R. Robinson, 1978: Energy analysis of open regions of turbulent flows—Mean eddy energetics of a numerical ocean circulation experiment. *Dyn. Atmos. Oceans*, **2**, 185–211, https://doi.org/10.1016/0377-0265(78)90009-X.

Holland, W. R., 1978: The role of mesoscale eddies in the general circulation of the ocean–numerical experiments using a wind-driven quasi-geostrophic model. *J. Phys. Oceanogr.*, **8**, 363–392, https://doi.org/10.1175/1520-0485(1978)008<0363:TROMEI>2.0.CO;2.

Hoskins, B. J., I. N. James, and G. H. White, 1983: The shape, propagation and mean-flow interaction of large-scale weather system. *J. Atmos. Sci.*, **40**, 1595–1612, https://doi.org/10.1175/1520-0469(1983)040<1595:TSPAMF>2.0.CO;2.

Kang, D., and E. N. Curchitser, 2015: Energetics of eddy-mean flow interactions in the Gulf Stream region. *J. Phys. Oceanogr.*, **45**, 1103–1120, https://doi.org/10.1175/JPO-D-14-0200.1.

Kundu, P. K., 1990: *Fluid Mechanics*. Academic Press, 638 pp.

Kushnir, Y., 1994: Interdecadal variations in North Atlantic sea surface temperature and associated atmospheric conditions. *J. Climate*, **7**, 141–157, https://doi.org/10.1175/1520-0442(1994)007<0141:IVINAS>2.0.CO;2.

Lorenz, E. N., 1955: Available potential energy and the maintenance of the general circulation. *Tellus*, **7**, 157–167, https://doi.org/10.1111/j.2153-3490.1955.tb01148.x.

Marshall, J., and T. Radko, 2003: Residual-mean solutions for the Antarctic Circumpolar Current and its associated overturning circulation. *J. Phys. Oceanogr.*, **33**, 2341–2354, https://doi.org/10.1175/1520-0485(2003)033<2341:RSFTAC>2.0.CO;2.

McCoy, D., D. Bianchi, and A. L. Stewart, 2020: Global observations of submesoscale coherent vortices in the ocean. *Prog. Oceanogr.*, **189**, 102452, https://doi.org/10.1016/j.pocean.2020.102452.

McDougall, T. J., and P. C. McIntosh, 2001: The temporal-residual-mean velocity. Part II: Isopycnal interpretation and the tracer and momentum equations. *J. Phys. Oceanogr.*, **31**, 1222–1246, https://doi.org/10.1175/1520-0485(2001)031<1222:TTRMVP>2.0.CO;2.

Munk, W., and C. Wunsch, 1998: Abyssal recipes II: Energetics of tidal and wind mixing. *Deep-Sea Res. I*, **45**, 1977–2010, https://doi.org/10.1016/S0967-0637(98)00070-3.

Okubo, A., 1970: Horizontal dispersion of floatable particles in the vicinity of velocity singularities such as convergences. *Deep-Sea Res. Oceanogr. Abstr.*, **17**, 445–454, https://doi.org/10.1016/0011-7471(70)90059-8.

Ollitrault, M., and A. Colin de Verdière, 2002: SOFAR floats reveal mid latitudes intermediate North Atlantic general circulation. Part II: An Eulerian statistical view. *J. Phys. Oceanogr.*, **32**, 2034–2053, https://doi.org/10.1175/1520-0485(2002)032<2034:SFRMIN>2.0.CO;2.

——, and J.-P. Rannou, 2013: ANDRO: An Argo-based deep displacement dataset. *J. Atmos. Oceanic Technol.*, **30**, 759–788, https://doi.org/10.1175/JTECH-D-12-00073.1.

——, and A. Colin de Verdière, 2014: The ocean general circulation near 1000-m depth. *J. Phys. Oceanogr.*, **44**, 384–409, https://doi.org/10.1175/JPO-D-13-030.1.

——, P. Rannou, E. Brion, C. Cabanes, A. Piron, G. Reverdin, and N. Kolodziejczyk, 2022: ANDRO: An Argo-based deep displacement dataset. SEANOE, accessed 20 April 2022, https://doi.org/10.17882/47077.

Owens, W. B., 1991: A statistical description of the mean circulation and eddy variability in the Northwestern Atlantic using SOFAR floats. *Prog. Oceanogr.*, **28**, 257–303, https://doi.org/10.1016/0079-6611(91)90010-J.

Phillips, H. E., and S. R. Rintoul, 2000: Eddy variability and energetics from direct current measurements in the Antarctic Circumpolar Current south of Australia. *J. Phys. Oceanogr.*, **30**, 3050–3076, https://doi.org/10.1175/1520-0485(2000)030<3050:EVAEFD>2.0.CO;2.

Rhines, P. B., and W. R. Holland, 1979: A theoretical discussion of eddy-driven mean flows. *Dyn. Atmos. Oceans*, **3**, 289–325, https://doi.org/10.1016/0377-0265(79)90015-0.

Rossby, H. T., S. C. Riser, and A. J. Mariano, 1983: The western North Atlantic—A Lagrangian viewpoint. *Eddies in Marine Science*, A. R. Robinson, Ed., Springer Verlag, 66–91.

Rossby, T., 1987: On the energetics of the Gulf Stream at 73W. *J. Mar. Res.*, **45**, 59–82, https://doi.org/10.1357/002224087788400918.

Saunders, P. M., and B. A. King, 1995: Bottom currents derived from a shipborne ADCP on WOCE cruise A11 in the South Atlantic. *J. Phys. Oceanogr.*, **25**, 329–347, https://doi.org/10.1175/1520-0485(1995)025<0329:BCDFAS>2.0.CO;2.

Sévellec, F., A. Colin de Verdière, and M. Ollitrault, 2017: Evolution of intermediate water masses based on Argo float displacement. *J. Phys. Oceanogr.*, **47**, 1569–1586, https://doi.org/10.1175/JPO-D-16-0182.1.

——, A. Naveira Garabato, and T. Huck, 2021: Damping of climate-scale oceanic variability by mesoscale eddy turbulence. *J. Phys. Oceanogr.*, **51**, 491–503, https://doi.org/10.1175/JPO-D-20-0141.1.

——, A. Colin de Verdière, and N. Kolodziejczyk, 2022: Estimation of horizontal turbulent diffusivity from deep Argo float displacements. *J. Phys. Oceanogr.*, **52**, 1509–1529, https://doi.org/10.1175/JPO-D-21-0150.1.

Starr, V. P., 1968: *Physics of Negative Viscosity Phenomena*. Mc Graw-Hill, 256 pp.

Tennekes, H., and J. L. Lumley, 1972: *A First Course in Turbulence*. MIT Press, 300 pp.

Tulloch, R., J. Marshall, and K. S. Smith, 2009: Interpretation of the propagation of surface altimetric observations in terms of planetary waves and geostrophic turbulence. *J. Geophys. Res.*, **114**, C02005, https://doi.org/10.1029/2008JC005055.

van Aken, H. M., H. van Haren, and L. R. M. Maas, 2007: The high-resolution vertical structure of internal tides and near-inertial waves measured with an ADCP over the continental slope in the Bay of Biscay. *Deep-Sea Res. I*, **54**, 533–556, https://doi.org/10.1016/j.dsr.2007.01.003.

van Sebille, E., L. M. Beal, and W. E. Johns, 2011: Advective time scales of Agulhas leakage to the North Atlantic in surface drifter observations and the 3D OFES model. *J. Phys. Oceanogr.*, **41**, 1026–1034, https://doi.org/10.1175/2011JPO4602.1.

von Storch, J.-S., C. Eden, I. Fast, H. Haak, D. Hernández-Deckers, E. Maier-Reimer, J. Marotzke, and D. Stammer, 2012: An estimate of the Lorenz energy cycle for the world ocean based on the 1/10° STORM/NCEP simulation. *J. Phys. Oceanogr.*, **42**, 2185–2205, https://doi.org/10.1175/JPO-D-12-079.1.

Wang, T., S. T. Gille, M. R. Mazloff, N. V. Zilberman, and Y. Du, 2020: Eddy-induced acceleration of Argo floats. *J. Geophys. Res. Oceans*, **125**, e2019JC016042, https://doi.org/10.1029/2019JC016042.

Waterman, S., and B. J. Hoskins, 2013: Eddy shape, orientation, propagation, and mean flow feedback in western boundary current jets. *J. Phys. Oceanogr.*, **43**, 1666–1690, https://doi.org/10.1175/JPO-D-12-0152.1.

——, and J. M. Lilly, 2015: Geometric decomposition of eddy feedbacks in barotropic systems. *J. Phys. Oceanogr.*, **45**, 1009–1024, https://doi.org/10.1175/JPO-D-14-0177.1.

Weiss, J., 1991: The dynamics of enstrophy transfer in two-dimensional hydrodynamics. *Physica D*, **48**, 273–294, https://doi.org/10.1016/0167-2789(91)90088-Q.

Whitehead, J. A., 1975: Mean flow generated by circulation on a β-plane: An analogy with the moving flame experiment. *Tellus*, **27A**, 358–364, https://doi.org/10.3402/tellusa.v27i4.9983.

Wunsch, C., and R. Ferrari, 2018: 100 years of the ocean general circulation. *A Century of Progress in Atmospheric and Related Sciences: Celebrating the American Meteorological Society Centennial*, *Meteor. Monogr.*, No. 59, Amer. Meteor. Soc., https://doi.org/10.1175/AMSMONOGRAPHS-D-18-0002.1.

Yan, X., D. Kang, E. N. Curchitser, and C. Pang, 2019: Energetics of eddy-mean flow interactions along the western boundary currents in the North Pacific. *J. Phys. Oceanogr.*, **49**, 789–810, https://doi.org/10.1175/JPO-D-18-0201.1.

Zhu, Y., B. Qiu, X. Lin, and F. Wang, 2018: Interannual eddy kinetic energy modulations in the Agulhas return current. *J. Geophys. Res. Oceans*, **123**, 6449–6462, https://doi.org/10.1029/2018JC014333.